SYNCHRONOUS DEMODULATION OF PIXELATED PHASE-SHIFTED INTERFEROGRAMS FOR DYNAMIC INTERFEROMETRY

M.Sc. José Moisés Padilla Miranda

"Synchronous Demodulation of Pixelated Phase-Shifted Interferograms for Dynamic Interferometry"

Thesis by:
M.Sc. José Moisés Padilla Miranda

In Partial Fulfillment of the Requirements for the Degree of:
Doctor of Science (Optics)

Dissertation advisers:
D.Sc. Manuel Servín Guirado
D.Sc. Julio Cesar Estrada Rico

León, Guanajuato, México. 2014.

Version definitiva.
Incluye cambios sugeridos por los revisores.

To my friends and family,
who often overlap.

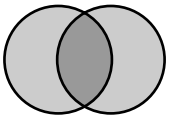

Abstract

Single-shot phase-shifting interferometers have become a *de facto* standard in interferometry for the study of fast dynamic phenomena and/or to achieve low-sensitivity to environmental vibrations. In particular, this dissertation work focuses on the study of pixelated phase-mask interferometers, which are commercially available solutions that encode four phase-shifted samples into a single-image pixelated-carrier interferogram.

The earliest phase-demodulation methods for pixelated-carrier interferograms used to rely on classic approaches such as the spatial Fourier demodulation and temporal phase-shifting algorithms (PSAs). However, implementing these phase-demodulation methods for pixelated-carrier interferograms has the following drawbacks: the input data needs to be rearranged in order to apply the algorithms, the quality of the estimated phase decreases due to an intrinsic approximation error on the demodulation method, and the resolution of the output signal is reduced to a quarter of the original one.

In 2010 it was demonstrated that the synchronous demodulation of pixelated-carrier interferograms has none of the above mentioned drawbacks. However, since the pixelated-carrier cannot be described as a linear function, additional work was required in order to assess this phase-demodulation method against the most commonly observed systematic errors in Interferometry: additive white-Gaussian noise (AWGN), detuning error and high-order distorting harmonics.

In this dissertation work are deduced the figures of merit of the synchronous demodulation method for pixelated phase-shifted interferograms, and two algorithmic approaches are proposed to cope with AWGN and detuning error. Moreover, two experimental variants are proposed to enhance the harmonic rejection capabilities of this technique: by increasing the number of the phase-shifted samples and by means of spatio-temporal phase demodulation.

Contents

List of used acronyms

AWGN	additive white-Gaussian noise
DTFT	discrete-time Fourier transform
FTF	frequency transfer function
LPF	low-pass filter
PPM	pixelated phase-mask
PPS	pixelated phase-shifting
PSA	phase shifting algorithm
LS-PSA	least-squares phase-shifting algorithm
PSI	phase shifting interferometry
SNR	(or S/N) signal-to-noise ratio

Chapter 1

Introduction

This chapter illustrates the importance of the single-shot phase-shifting interferometers in dynamic interferometry. Some of the basic concepts discussed below (such as the framework of inverse problems, phase ambiguities and quadrature linear filtering) may be particularly useful for beginning students in interferometry. This chapter also serves to establish the notation and conventions for the following chapters.

1.1 The inverse problem in interferometry

In interferometry, a fringe pattern is usually defined as a sinusoidal signal where a continuous map, analogous of the physical quantity being measured, is phase-modulated by an interferometer, Moire' system, etc. A useful mathematical model for an ideal and stationary fringe pattern is given by

$$I(x,y) = a(x,y) + b(x,y)\cos[\varphi(x,y)]\,, \tag{1.1}$$

where $a(x,y)$ represents a background signal, $b(x,y)$ is the local contrast function, and $\varphi(x,y)$ is the searched phase under study.

In physics and mathematics, the process of converting measurements into information about a phenomenon under study is called an inverse problem. Moreover, an inverse problem is well-posed *if and only if* its mathematical model fulfills the next conditions [38]:

1. A solution exists,

2. The solution is unique, and

3. The solution depends continuously on the data.

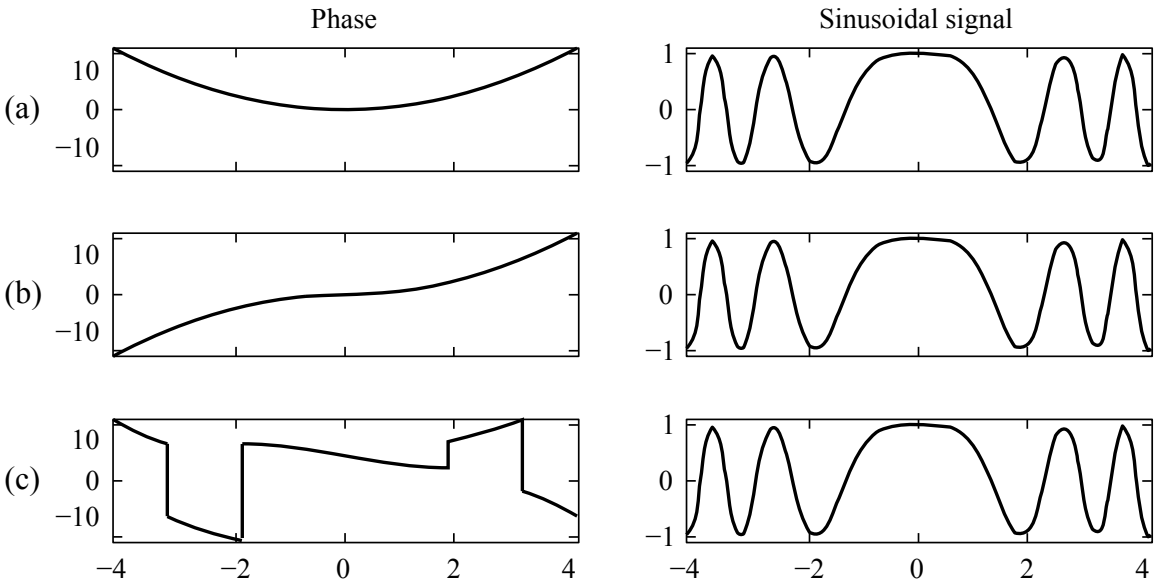

Figure 1.1: Numerical simulation of several phases (left), from an infinite number of possibilities, producing exactly the same sinusoidal signal (right). For ease of observation, only a horizontal slice is shown.

Analyzing these conditions, it is clear that Eq. 1.1 represents an inverse problem where the fringe pattern $I(x,y)$ is our measurement and the searched information is given by the phase map $\varphi(x,y)$. Particularly, this is an ill-posed inverse problem since the phase function $\varphi(x,y)$ cannot be directly estimated because it is screened by the unknown functions $a(x,y)$ and $b(x,y)$. Moreover, in all practical cases there is an amount of additive and/or multiplicative noise, $n(x,y)$, and the fringe pattern may suffer from non-linear distortions degrading its quality and adding more screening into the phase information (for more details see [7, 30]).

In addition to the screening by the unknown signals, $\{a(x,y),\ b(x,y),\ n(x,y)\}$, it is important to notice that $\varphi(x,y)$ can only be determined modulo 2π because the sinusoidal fringe pattern $I(x,y)$ depends periodically on the phase; this is called a 2π phase ambiguity. Also, its sign cannot be extracted from a single measurement due to the even character of the cosine function; this is called sign ambiguity. Even if a controlled experimental setup prevents the screening of $\varphi(x,y)$ due to the unknown signals, one still have to deal with the sign and the 2π phase ambiguities. Thus, the solution for this inverse problem is not unique as it is illustrated in Fig. 1.1.

Finally, the phase demodulation from a fringe pattern can be viewed as an ill-posed inverse problem where additional information needs to be provided (i.e., to perform some regularization process) in order to obtain a proper phase estimation.

1.1.1 Adding *a priori* information to the fringe pattern: carriers

A fringe pattern obtained as the output signal for a measuring system can be modified by an optoelectronic-mechanical hardware (sensors and actuators) and/or software (virtual sensors and actuators) [15]. With these modifications is possible to introduce the following change in the argument of the sinusoidal signal:

$$I(x,y,t) = a(x,y) + b(x,y)\cos[\varphi(x,y) + c(x,y,t)]\,, \tag{1.2}$$

where $c(x,y,t)$ is a *known* function called the spatio-temporal carrier of the interferogram. Since in general $\cos(\varphi + c) \neq \cos(-\varphi + c)$, it is clear that this carrier function solves the sign ambiguity. By itself, this is a good step towards turning the inverse problem from ill-posed to well-posed. Since the carrier function is assumed to be known, the so-called synchronous demodulation method allows us to straightforwardly solve the screening problem as it is shown next.

In the context of the analysis of fringe patterns and digital interferometry, the adjective *synchronous* means that the modulating carrier is known. This term was adopted from communication techniques (such as the amplitude modulation, the phase modulation and the single-sideband modulation) where the input signal is mixed (multiplied) with a local oscillator tuned at the carrier's frequency, and then the output is low-pass filtered in order to recover the encoded information.

Applying Euler's formula for the cosine function in Eq. 1.2, we have:

$$\begin{aligned} I(x,y,t) = a(x,y) &+ (1/2)b(x,y)\exp\{i[\varphi(x,y) + c(x,y,t)]\} \\ &+ (1/2)b(x,y)\exp\{-i[\varphi(x,y) + c(x,y,t)]\}\,. \end{aligned} \tag{1.3}$$

Taking the synchronous product $I(x,y,t)\exp[-ic(x,y,t)]$ results:

$$\begin{aligned} I(x,y,t)\exp[-ic(x,y,t)] = a(x,y)\exp[-ic(x,y,t)] &+ (1/2)b(x,y)\exp[i\varphi(x,y)] \\ &+ (1/2)b(x,y)\exp\{-i[\varphi(x,y) + 2c(x,y,t)]\}\,. \end{aligned} \tag{1.4}$$

By design, the carrier frequency must be higher than the frequency of the searched phase:

$$\left|\frac{\partial c}{\partial x}\right| > \left|\frac{\partial \varphi}{\partial x}\right|_{\max}, \quad \left|\frac{\partial c}{\partial y}\right| > \left|\frac{\partial \varphi}{\partial y}\right|_{\max}, \quad \left|\frac{\partial c}{\partial t}\right| > \left|\frac{\partial \varphi}{\partial t}\right|_{\max}. \tag{1.5}$$

The only low-frequency signal in Eq. 1.4 is the searched analytic signal $(b/2)\exp(i\varphi)$. Thus, applying a low-pass filter (LPF) to the synchronous product we are able to reject the high-frequency terms modulated by the $\exp[-ic(x,y,t)]$ and the $\exp[-i2c(x,y,t)]$ terms, resulting:

$$LPF\{I(x,y,t)\exp[-ic(x,y,t)]\} = (1/2)b(x,y)\exp[i\hat{\varphi}(x,y)], \tag{1.6}$$

where the "hat" (^) indicates an estimated value. This analytic signal contains both magnitude and phase, but we are only interested in the later which can be computed as follows:

$$\hat{\varphi}(x,y) \bmod 2\pi = \tan^{-1}\left(\frac{\mathrm{Im}\{(1/2)b(x,y)\exp[i\varphi(x,y)]\}}{\mathrm{Re}\{(1/2)b(x,y)\exp[i\varphi(x,y)]\}}\right), \tag{1.7}$$

As can be seen, this result is wrapped within a single branch due to the arc-tangent operation, i.e. $\hat{\varphi}(x,y) \in (-\pi,\pi)$. Thus, we conclude that the phase carrier solves the screening problem and the sign ambiguity but not the 2π phase ambiguity.

There are many algorithmic approaches to unwrap our estimated phase –the final step before achieving a well-posed inverse problem– in order to obtain $\hat{\varphi}(x,y) \in \mathbb{R}^2$. However, the phase unwrapping process has its own set of challenges and entire books have been written on this topic (see for instance [9]). For our purposes it suffices to say that the unwrapping process is trivial for phase maps calculated from good-quality fringe data; in such phase maps, the absolute phase difference between adjacent pixels is less tan π radians except for the expected 2π discontinuities [9, 35].

For further illustration of the synchronous demodulation method, in the following sections will be analyzed the most commonly used carrier modulations in interferometry: the spatial linear carrier, given by $u_0x + v_0y$; and the temporal linear carrier, given by $\omega_0 t$.

1.2 Spatial linear carrier modulation

The spatial linear carrier modulation technique in interferometry was demonstrated by Ichioka and Inuiya [11] in 1972, and later popularized by Takeda et al. [37] in 1982. This technique usually involves wavefront splitting and different propagation paths (one for the test arm and another for the reference one) which enable to introduce a tilt in the optical path difference resulting in a spatial linear carrier modulation of the form $u_0x + v_0y$.

As it was discussed in the previous section, the inclusion of a known carrier solves the sign ambiguity (actually, at the moment of its publication this feature was highlighted as one of the main advantages of this technique) [11, 37]. Moreover, if the carrier frequency is higher than the frequency of the searched phase, this spatial linear carrier modulation

also solves the screening problem. A useful mathematical model for a spatial linear carrier modulated interferogram is given by:

$$I(x,y) = a(x,y) + b(x,y)\cos[\varphi(x,y) + u_0 x + v_0 y], \tag{1.8}$$

where $\{u_0, v_0\}$ are assumed to be known or can be easily calculated from the fringe pattern, and all other parameters remain as previously defined. Taking $v_0 = 0$ in order to simplify the analysis and applying Euler's formula in Eq. 1.8, we have:

$$\begin{aligned} I(x,y) = a(x,y) &+ \{(1/2)b(x,y)\exp[i\varphi(x,y)]\}\exp(iu_0 x) \\ &+ \{(1/2)b(x,y)\exp[-i\varphi(x,y)]\}\exp(-iu_0 x). \end{aligned} \tag{1.9}$$

Note that the terms enclosed by braces are unknown functions. For simplicity, let's rename them as

$$\begin{aligned} c(x,y) &= (1/2)b(x,y)\exp[i\varphi(x,y)], \\ c^*(x,y) &= (1/2)b(x,y)\exp[-i\varphi(x,y)], \end{aligned} \tag{1.10}$$

where the asterisk denote the complex conjugate. Then, taking the 1-D Fourier transform of Eq. 1.9 in the $x-$direction, we have[1]:

$$\mathscr{F}_x\{I(x,y)\} = I(u,y) = A(u,y) + C(u-u_0,y) + C^*(u+u_0,y). \tag{1.11}$$

As it is illustrated in the Fig. 1.2, the spectrum of this spatial linear carrier interferogram is composed by separated and non-overlapped spectral lobes *if* the bandwidth of $A(u,y)$ and $C(u,y)$ is smaller than u_0 radians. In practice, $a(x,y)$ and $b(x,y)$ represent low-frequency signals, so this condition is usually imposed on the phase as [11, 37]:

$$\left|\frac{\partial\varphi}{\partial x}\right|_{\max} < u_0. \tag{1.12}$$

If the above condition is fulfilled, the fringes observed in a spatial linear carrier interferogram will be open. For this reason, a spatial linear carrier interferogram is also commonly referred as an open-fringes pattern.

Thanks to the spectral separation between the components of $I(u,y)$, it is possible to isolate the searched analytic signal by two similar (but not completely equivalent) synchronous methods. The first approach consists in spectrally displace the entire spectrum by

[1] To deduce this result, the following properties of the Fourier transform were applied: $\mathscr{F}\{f(x)\} = F(u)$, $\mathscr{F}\{f(x)\exp(iu_0 x)\} = F(u-u_0)$, and $\mathscr{F}\{f^*(x)\} = F^*(-u)$.

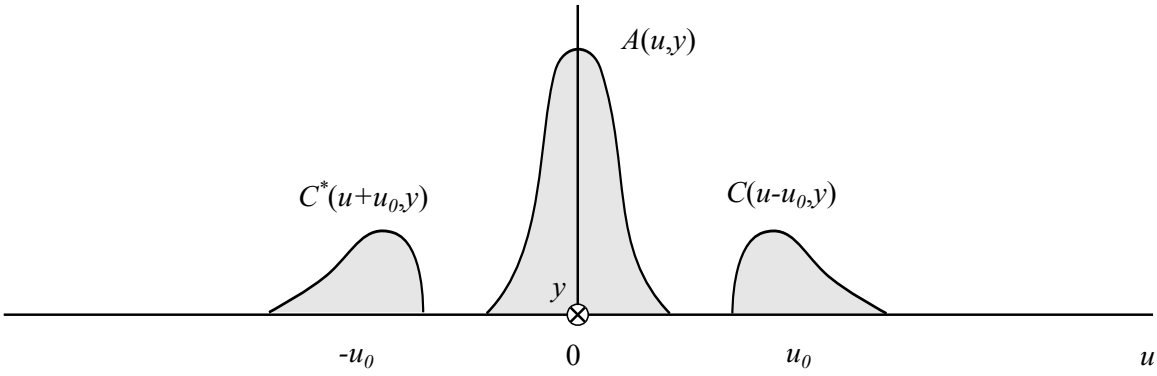

Figure 1.2: Schematic Fourier spectrum of an (open-fringes) interferogram with spatial linear carrier modulation.

means of the synchronous product, $I(x,y,t)\exp(-iu_0x)$, resulting:

$$I(x,y)\exp(-iu_0x) = a(x,y)\exp(-iu_0x) + (1/2)b(x,y)\exp[i\varphi(x,y)] + (1/2)b(x,y)\exp\{-i[\varphi(x,y)+2u_0x]\}, \quad (1.13)$$

Following the previously established notation $c(x,y) = (1/2)b(x,y)\exp[i\varphi(x,y)]$, the above equation is given in the Fourier domain by:

$$I(u-u_0,y) = A(u+u_0,y) + C(u,y) + C^*(u+2u_0,y). \quad (1.14)$$

As it is illustrated in the Fig. 1.3, this means that only the searched analytic signal remains in the base-band after taking the synchronous product $I(x,y,t)\exp(-iu_0x)$. Then, we are able to isolate this analytic signal by means of conventional low-pass filtering:

$$\begin{aligned} LPF\{I(u-u_0,y)\} &= C(u,y), \\ LPF\{I(x,y)\exp(-iu_0x)\} &= (1/2)b(x,y)\exp[i\varphi(x,y)]. \end{aligned} \quad (1.15)$$

As it was demonstrated in the previous section, it is straightforward to solve the above result for the searched phase by computing the angle of this analytic signal (see Eq. 1.7). Thus, when reaching this point we say that the inverse problem of phase-demodulating an open-fringes interferogram is solved (except for the 2π ambiguity).

Before analyzing the second phase-demodulation approach for open-fringes interferograms, it is necessary to define a filter's action by means of the convolution with its impulse response function, $h(x,y)$. That is:

$$LPF\{I(x,y)\} = I(x,y) * h(x,y). \quad (1.16)$$

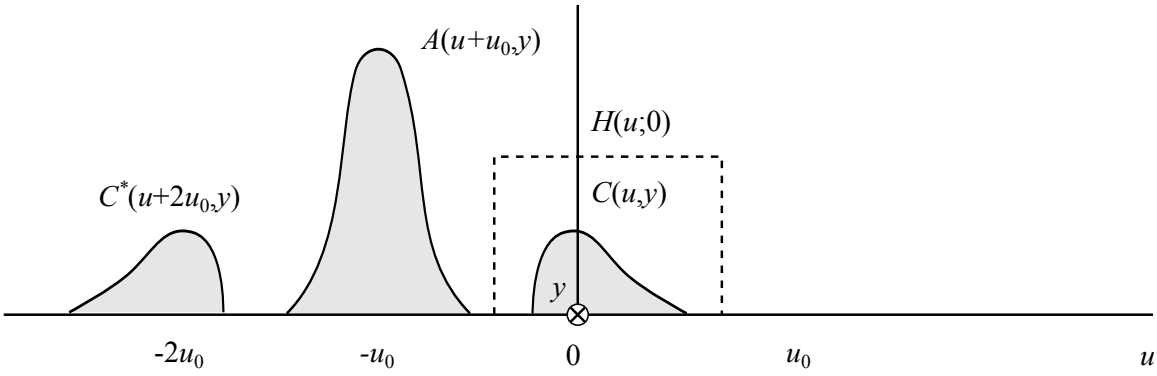

Figure 1.3: Schematic Fourier spectrum of the synchronous demodulation of an open-fringes interferogram by means of low-pass linear filtering (tuned at $u = 0$).

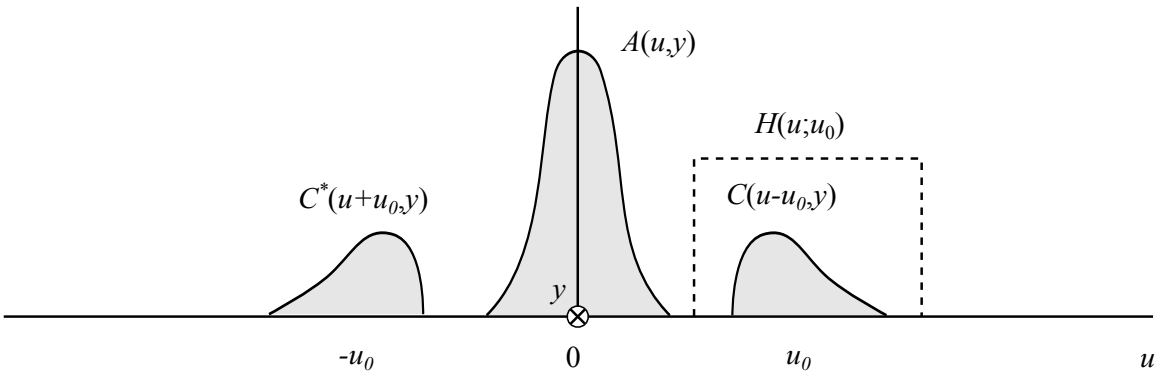

Figure 1.4: Schematic Fourier spectrum of the synchronous demodulation of an open-fringes interferogram by means of complex-valued quadrature linear filtering (tuned at $u = u_0$).

This definition is valid under the assumption of a linear time-invariance, and the prototypical example for this definition are the averaging masks for low-pass filtering. Now, we can define a quadrature linear filter (QLF) tuned at $u = u_0$ as follows:

$$QLF\{I(x,y)\} = I(x,y) * [h(x,y)\exp(iu_0x)]\,. \tag{1.17}$$

In other words, quadrature linear filters are complex-valued and, in general, they are given by the combination of the synchronous product and a low-pass filtering. Moreover, analyzing in the Fourier domain we have:

$$\mathscr{F}_x\{I(x,y) * [h(x,y)\exp(iu_0x)]\} = I(u,y)H(u-u_0)\,. \tag{1.18}$$

As it is illustrated in Fig. 1.4, the above equation means that with quadrature linear filtering now we are spectrally displacing the filter's spectrum instead of the spectrum of the open-

fringes interferogram. Proceeding as before it is easy to prove that:

$$I(x,y) * [h(x,y)\exp(iu_0x)] = (1/2)b(x,y)\exp[i\varphi(x,y) + iu_0x]\,. \tag{1.19}$$

By comparing the Eq. 1.15 and the Eq. 1.19, it is clear that the second approach has the drawback of requiring an extra step to remove the linear term u_0x from the estimated phase. For illustrative purposes, two numerical simulations will be shown in Fig. 1.6 and Fig. 1.7. **However, before proceeding any further it is important to describe the main features of the numerical simulations that will be used throughout this dissertation work:**

- Unless explicitly stated otherwise, the spatial resolution is 512×512 pixels.
- The amplitude of fringe patterns and wrapped phases is linearly mapped with 256 shades of gray (8-bit range). For the fringe patterns, the black color equals 0 bits and the white color equals 256 bits. Similarly for the wrapped phases, the black color equals $-\pi$ radians and the white color equals π radians. On the other hand, the Fourier spectrum plots are in pseudo-color logarithmic-intensity scale with the minimum value mapped in blue and the maximum in red. See Fig. 1.5.
- The Fourier spectrum plots are first computed with the `fft2`$(\cdot)$ algorithm, and next these are shifted using `fftshift`$(\cdot)$ to have the spectral origin at the center of the image. Their axis are within the principal branch $(u,v) \in (-\pi,\pi] \times (-\pi,\pi]$.

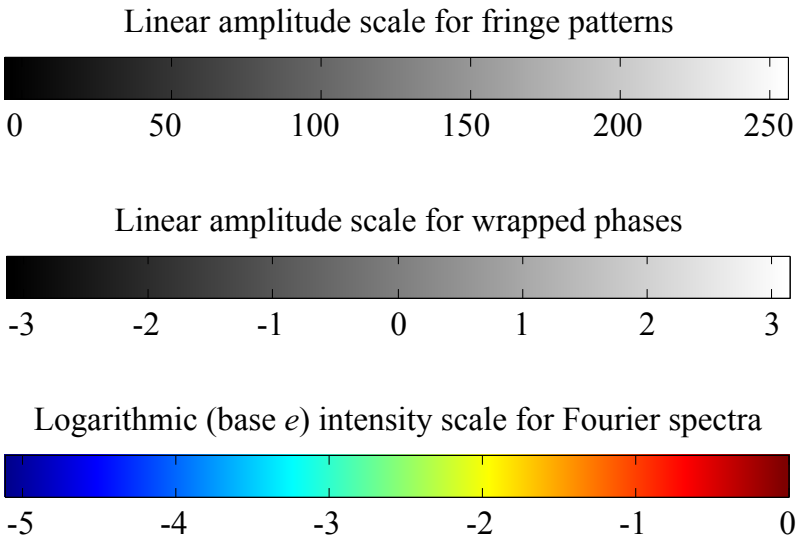

Figure 1.5: Pseudo-color scale bars for the numeric simulations in this dissertation work.

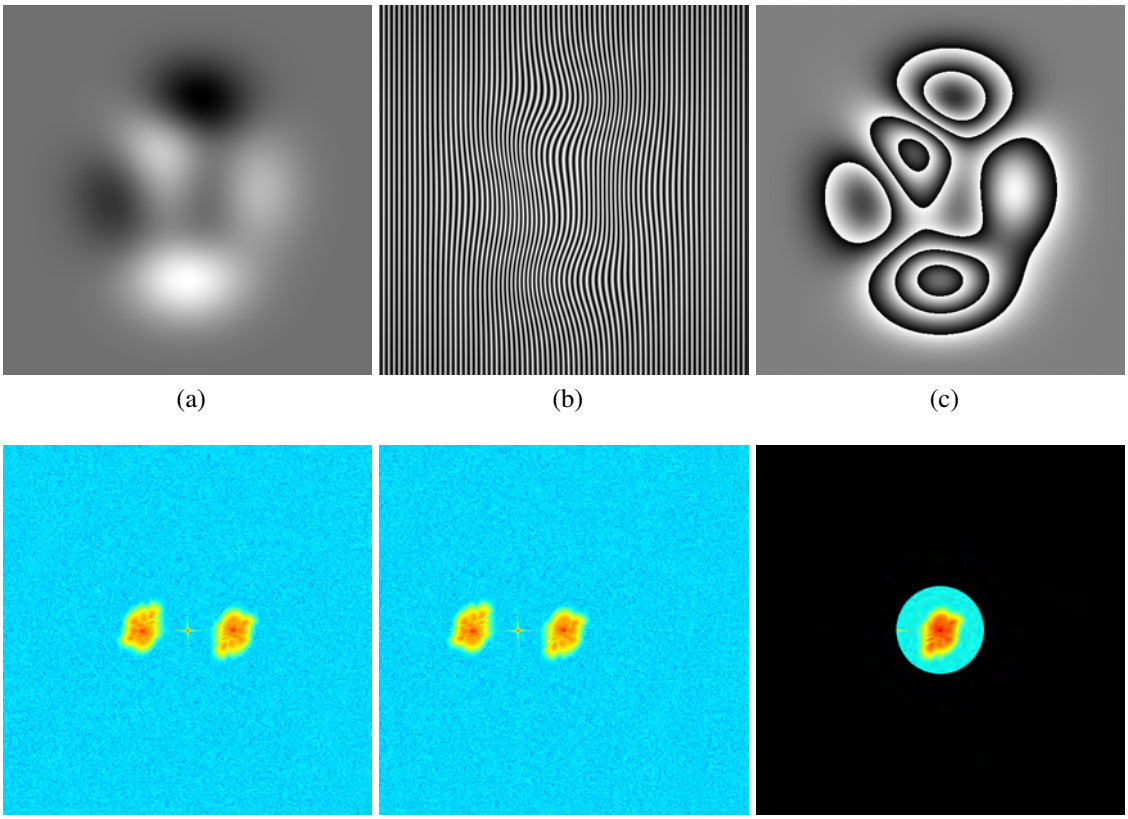

(a) (b) (c)

(d) (e) (f)

Figure 1.6: Low-pass linear filtering phase-demodulation of an open-fringes interferogram. Panel (a) shows the computer modulated phase we want to recover from the open fringes interferogram in panel (b). Panel (c) shows the estimated phase modulo 2π obtained with the synchronous demodulation method and linear filtering at the base-band. Panels (d-f) show respectively the Fourier spectra of $I(x,y)$, $I(x,y)\exp(-iu_0x)$ and $LPF\{I(x,y)\exp(-iu_0x)\}$, with the spectral origin at the image center.

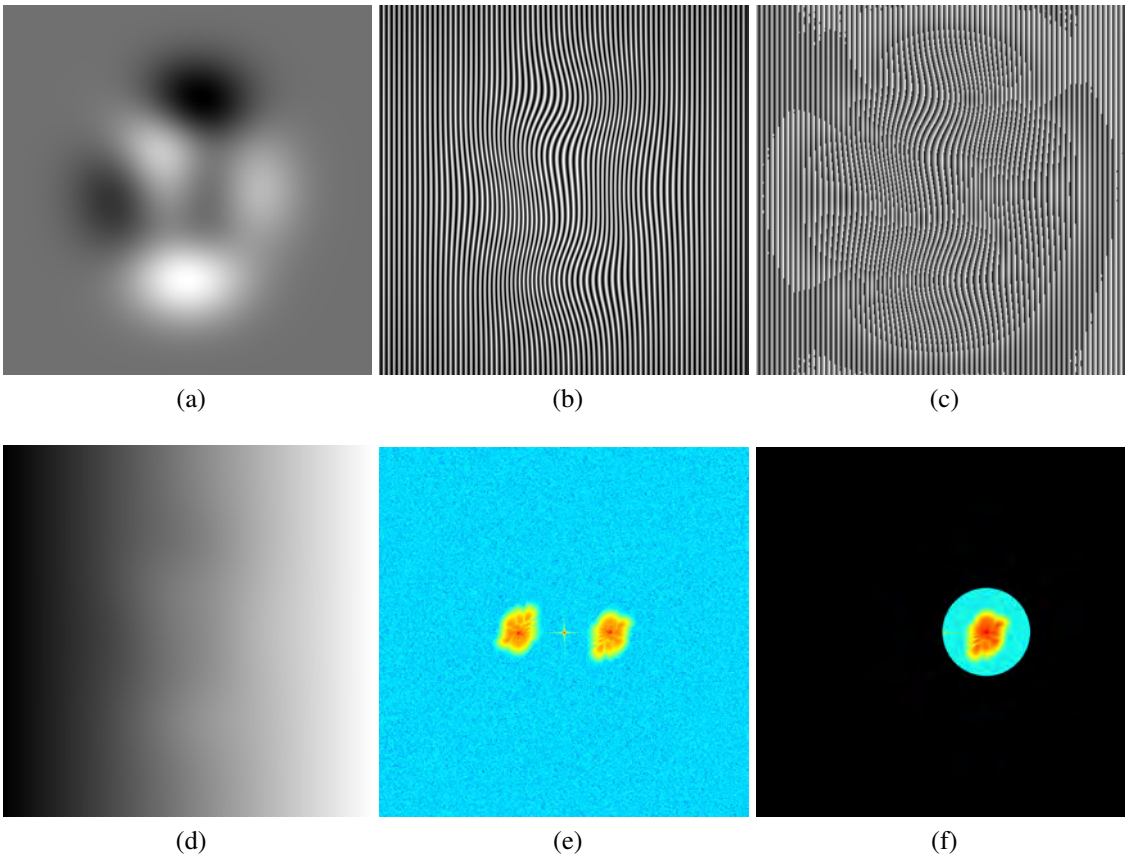

Figure 1.7: Quadrature linear-filtering demodulation of an open-fringes interferogram. Phase demodulation of an interferogram with spatial linear carrier modulation. Panel (a) shows the computer modulated phase we want to recover from the open fringes interferogram in panel (b). Panel (c) shows the estimated phase modulo 2π obtained with quadrature linear filtering around $u = u_0$. Panel (d) shows the estimated phase $\hat{\varphi}(x,y) + u_0 x$, obtained after the unwrapping process. Panels (e-f) show respectively the Fourier spectra of $I(x,y)$, and $\{I(x,y) * [h(x,y)\exp(iu_0 x)]\}$, with the spectral origin at the image center.

By comparison of Panel 1.6(c) and Panel 1.7(c), it is clear that the quadrature linear filtering approach requires an extra step to remove the linear term $u_0 x$ from the estimated phase (as predicted by the theory). For this reason, when working with spatial linear carrier modulation is preferable to first take the synchronous product $I(x,y)\exp(-iu_0 x)$ and then apply a linear low-pass filtering at the base-band.

Being able to demodulate open-fringe patterns from a single image, and the fact that once calibrated it uses no moving components, makes this technique particularly useful to study fast-dynamic phenomena [11, 37]. Nevertheless, the condition for no spectral overlapping $(\max|\varphi_x| < u_0)$ effectively restricts the applicability of this technique to low-frequency phase maps and/or very high frequency modulating carriers.

1.3 Temporal linear carrier modulation

The pioneer techniques for temporal linear carrier modulation in interferometry were proposed by P. Carré [5] and R. Crane [6] at the late 1960s. However, the synchronous demodulation method for temporal phase-shifted interferograms was not exploited until 1974 when it was demonstrated by Bruning et al. [4]. Following these pioneer works [4, 5, 6], several researchers proposed alternative experimental approaches to improve the flexibility and reliability while simultaneously developing a more robust demodulation theory (for more details see for instance [29, 33]), and nowadays this is still an open-research topic.

A very popular technique to produce temporal linear carrier modulation is the moving reference mirror where one of the arms of the interferometer is continuously displaced in order to introduce incremental phase-steps between successive samples of the interferometric signal:

$$\begin{aligned} I_0(x,y) &= a(x,y)+b(x,y)\cos[\varphi(x,y)]\,, \\ I_1(x,y) &= a(x,y)+b(x,y)\cos[\varphi(x,y)+\omega_0]\,, \\ I_2(x,y) &= a(x,y)+b(x,y)\cos[\varphi(x,y)+2\omega_0]\,, \\ &\vdots \end{aligned} \tag{1.20}$$

where ω_0 (in radians per sample) is the so-called phase-step. Clearly, the above set of equations can be described as a single temporal signal as:

$$I(x,y,t) = a(x,y)+b(x,y)\cos[\varphi(x,y)+\omega_0 t]\,, \tag{1.21}$$

where $a(x,y)$ represents the background, $b(x,y)$ is the fringe's contrast function, $\varphi(x,y)$ is the searched phase, and $\omega_0 t$ represents the temporal linear carrier phase modulation.

Taking the temporal Fourier transform of $I(x,y,t)$, we have:

$$\begin{aligned} I(x,y,\omega) =& a(x,y)\delta(\omega)+(1/2)b(x,y)\exp[i\varphi(x,y)]\delta(\omega-\omega_0) \\ &+(1/2)b(x,y)\exp[-i\varphi(x,y)]\delta(\omega+\omega_0)\,. \end{aligned} \tag{1.22}$$

As illustrated in Fig. 1.8, the previous equation means that temporal-carrier modulation produces spectral separation between the component signals of the interferogram. Moreover, since $\{a,b,\varphi\}$ do not have temporal dependency, the spectral lobes are given by infinitely thin spikes; that is, by Dirac delta functions.

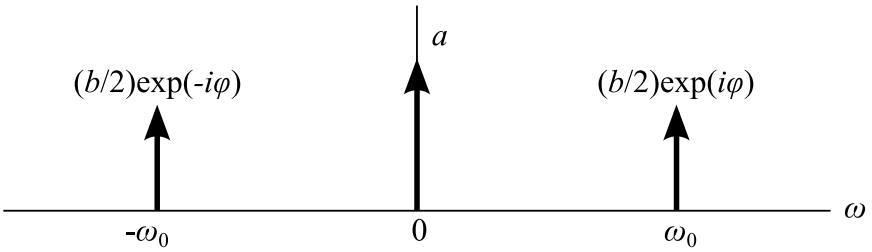

Figure 1.8: Spectrum of an ideal temporal linear carrier interferogram. The vertical axis has arbitrary units.

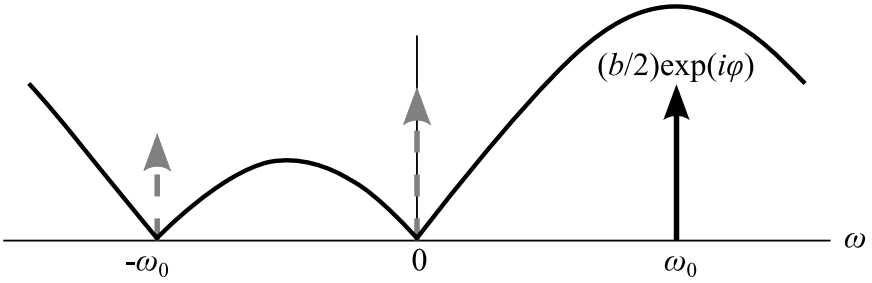

Figure 1.9: Spectrum of an ideal temporal linear carrier interferogram after being demodulated using a 3-step quadrature linear filter (the continuous line corresponds to its frequency transfer function $H(\omega)$). The vertical axis has arbitrary units.

Following the synchronous demodulation method there are two alternatives to isolate the searched analytical signal $(1/2)b(x,y)\exp[i\varphi(x,y)]$: by spectrally displacing the data and using a real-valued low-pass filter, or by applying a (complex-valued) quadrature linear filter. The second approach is more commonly found in the specialized literature: Nevertheless, for temporal linear carrier modulation both approaches produce identical results up-to an irrelevant phase piston (for more details see for instance [33]). Analyzing Eq. 1.22, it is clear that we can isolate the searched analytic signal $(1/2)b(x,y)\exp[i\varphi(x,y)]$ with a quadrature linear filter, given by

$$h(t) = \sum c_n \delta(t-n), \quad \{c_n\} \in \mathbb{C}, \tag{1.23}$$

if its frequency transfer function $H(\omega) = \mathscr{F}\{h(t)\}$ fulfills the so-called quadrature conditions [8, 33, 36]:

$$H(0) = H(-\omega_0) = 0\,, \quad H(\omega_0) \neq 0\,. \tag{1.24}$$

This is illustrated in the Fig. 1.9. Thus, applying this quadrature linear filtering to Eq. 1.22 we have in the Fourier domain:

$$I(\omega)H(\omega) = (1/2)H(\omega_0)b(x,y)\exp[i\varphi(x,y)]\delta(\omega-\omega_0)\,. \tag{1.25}$$

Which can be translated to the temporal domain as:

$$I(t) * h(t) = \sum c_n I(t-n) = \frac{1}{2} b(x,y) H(\omega_0) \exp i[\hat{\varphi}(x,y) + \omega_0 t] \,. \tag{1.26}$$

From this analytic signal, the searched phase $\hat{\varphi}(x,y)$ can be computed from its angle, and the fringe's contrast function $b(x,y)$ –which is particularly important in quality-guided phase unwrapping– is directly proportional to its magnitude. The coefficients $\{c_n\}$ depend on the specific quadrature linear filter to be applied. For instance, for the well-known 4-step (least-squares) phase shifting algorithm by Bruning et al. [4] and James C. Wyant [39] it is given in analytic formulation by:

$$A_0(x,y) \exp[i\hat{\varphi}(x,y)] = I_0(x,y) - iI_1(x,y) - I_2(x,y) + iI_3(x,y) \,. \tag{1.27}$$

The advantage of using temporal linear carrier modulation is that no restrictions on the spatial frequencies of the signal under study are imposed –apart from being above the Nyquist limit in order to avoid the aliasing phenomenon– so we are able work with closed-fringes interferograms. On the other hand, this technique cannot be applied to dynamic phenomena since we require that at least the phase under study remains fixed over the entire time it takes to capture all the phase-shifted interferograms. Nevertheless, there are several approaches for single-shot phase-shifting interferometry[2], and in fact the main subject of this dissertation work are state-of-the-art demodulation methods for one of these techniques.

For completeness, some illustrative numerical simulations with temporal linear carrier modulation are shown next (see Fig. 1.10). For this simulation were generated three phase-shifted interferograms with a relative step of $\omega_0 = 2\pi/3$ radians per sample. As it was assumed in the previously discussed theory, there was no temporal variation in the background signal, the local contrast function and the searched phase map. For illustrative purposes both approaches for the phase demodulation of closed-fringes interferograms were applied: a synchronous product with (real-valued) low-pass filtering and (complex-valued) quadrature linear filtering.

[2]For more details see for instance chapter 11 in *Optical Metrology* by Kjell J. Gåsvik [10].

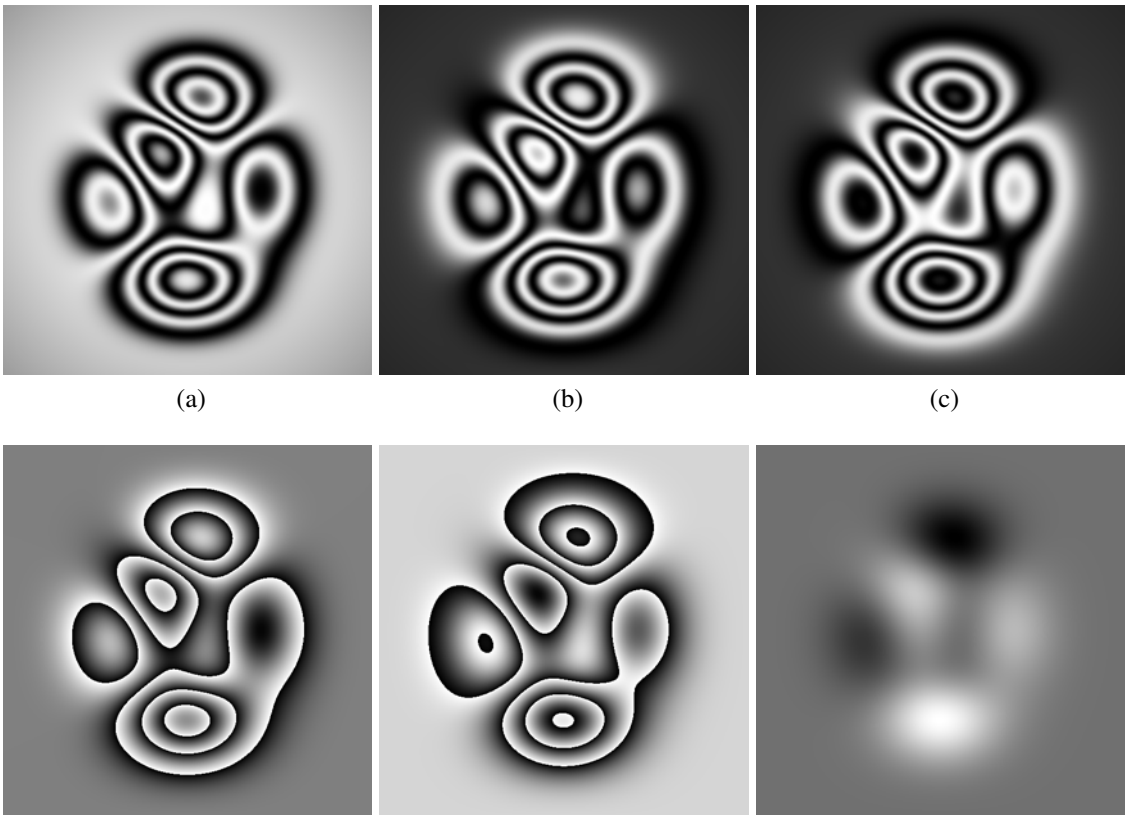

(a) (b) (c)

(d) (e) (f)

Figure 1.10: Phase demodulation of an interferogram with temporal linear carrier modulation. Panels (a-c) show the closed-fringes interferograms, i.e. the input data, with a relative phase-step $\omega_0 = 2\pi/3$. The wrapped phase in panel (d) was obtained with quadrature linear filtering, while in panel (e) was obtained by spectrally displacing the data and using a real-valued low-pass filter; the only difference between both results is an irrelevant phase-piston of $2\pi/3$. Panel (g) shows the estimated phase $\hat{\varphi}(x,y)$ as obtained after the unwrapping process.

To summarize:

The spatial linear carrier modulation is particularly useful to study fast-dynamic phenomena but the condition for no-spectral overlapping $(\max|\varphi_x| < u_0)$ restricts its application to low-frequency phase maps and/or very high-frequency carriers [11, 37].

On the other hand, temporal linear carrier modulation does not restrict the spatial frequencies of the signal under study, so we are able work with closed-fringes interferograms. However, the classical approach for temporal linear carrier modulation cannot be applied to dynamic phenomena because we require the phase under study to remain fixed over the entire time it takes to capture all the phase-shifted interferograms [4].

Chapter 2

Pixelated phase-shifting (PPS)

In this chapter is discussed a single-shot technique known as pixelated phase-shifting modulation, and we will analyze three alternative methods for its phase-demodulation. The first two methods rely on information rearrange in order to use "conventional" phase-shifting algorithms or the spatial Fourier method. The third method, the so-called synchronous phase demodulation, have at least two major advantages since does not require any information rearrange and allows us to make better use of the available spectral space.

2.1 Pixelated phase-shifted modulation

Originally demonstrated in 2003 by Brock et al. [2], the pixelated phase-shifted modulation is a single-shot phase-shifting technique that allow us to remove the applicability restrictions of the spatial and temporal linear carrier techniques discussed in the previous chapter; that is, with this technique we are able to demodulate closed-fringe patterns generated by fast-dynamic phenomena (which in principle it is impossible to analyze with the Fourier method or with temporal phase-shifting interferometry).

As it is illustrated in Fig. 2.1, the pixelated phase-shifted technique requires a polarization interferometer that generates a reference wavefront and a test wavefront having orthogonal polarization states with respect to each other; then the pixelated phase-mask (a periodic array of micro-polarizers that interfere the transmitted light) introduces a specific phase-delay for each pixel on a CCD image sensor, resulting on a very high-frequency carrier modulation. The physical principles for this technique are described in Ref. [2, 21].

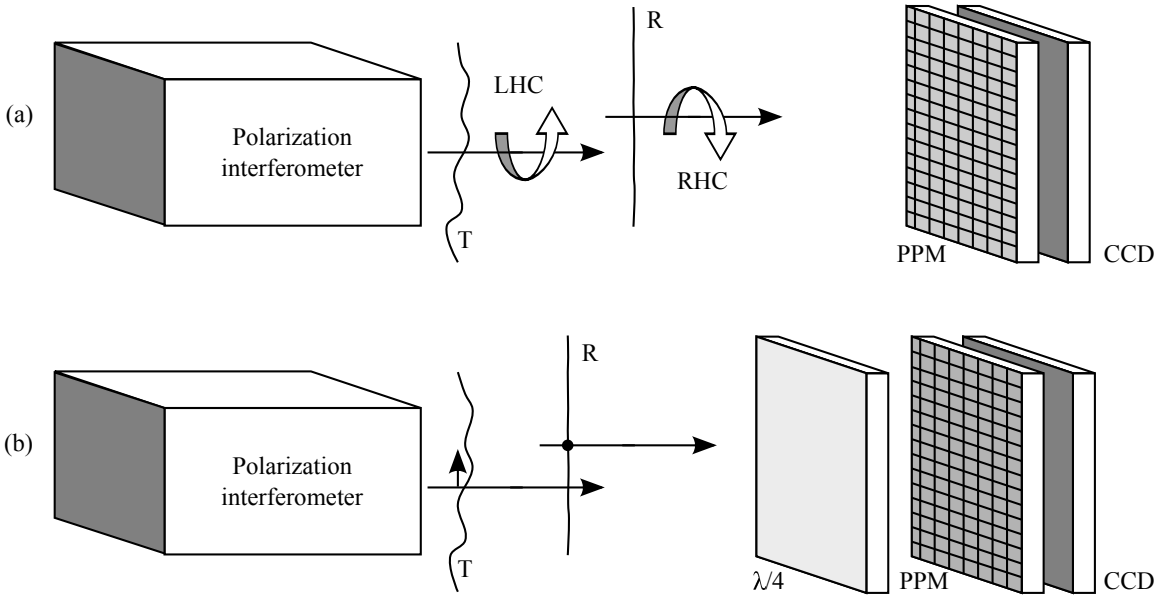

Figure 2.1: Basic schemes for the pixelated phase-mask (PPM) interferometer. In panel (a) the reference and test beams have orthogonal circular polarizations. For the use of linearly polarized beams, as shown in panel (b), a quarter-wave retardation plate is required.

According to Brock et al. [2, 3] and Millerd et al. [19, 21], the pixelated phase-mask interferometer method has the following advantages in comparison to conventional temporal phase-shifting interferometry and alternative single-shot phase-shifting solutions:

> "1) A true common path arrangement permits the use of broadband or white light and minimizes aberrations; 2) extremely compact design; 3) achromatic over a very wide range; and 4) fixed spatial interference pattern results in fast processing."

The pixelated phase-mask technique is implemented in commercially available single-shot interferometers by 4D Technology Corporation, where four phase-steps $\{0, \pi/2, \pi, 3\pi/2\}$ are acquired simultaneously "in as little as thirty microseconds" and encoded in the interferogram as follows:

$$I(x,y) = a(x,y) + b(x,y)\cos[\varphi(x,y) + c(x,y)]\,, \tag{2.1}$$

where, as usual, $a(x,y)$ and $b(x,y)$ represent the background and local contrast functions, $\varphi(x,y)$ is the searched phase function under study and $c(x,y)$ is a non-linear 2D carrier with very high spatial-frequency (with variations of up-to $3\pi/2$ radians between adjacent

pixels). For instance, for the so-called circular orientation [12], $c(x,y)$ is given by:

$$c(x,y) = \frac{\pi}{2}\begin{bmatrix} 0 & 1 & 0 & 1 & \dots \\ 3 & 2 & 3 & 2 & \dots \\ 0 & 1 & 0 & 1 & \dots \\ 3 & 2 & 3 & 2 & \dots \\ \vdots & \vdots & \vdots & \vdots & \ddots \end{bmatrix}. \tag{2.2}$$

Clearly, this 2D pixelated carrier represents a periodic array with a 2×2 unit-cell or "super-pixel", $\mathbf{s}(x,y)$, containing the four phase-step values $\{0, \pi/2, \pi, 3\pi/2\}$. In this dissertation work will be considered three possibilities: the so-called "stacked", "circular" and linear configurations, where $\mathbf{s}(x,y)$ is given respectively by:

$$\mathbf{s}_{stacked}(x,y) = \frac{\pi}{2}\begin{bmatrix} 0 & 1 \\ 2 & 3 \end{bmatrix}, \tag{2.3}$$

$$\mathbf{s}_{circular}(x,y) = \frac{\pi}{2}\begin{bmatrix} 0 & 1 \\ 3 & 2 \end{bmatrix}, \tag{2.4}$$

$$\mathbf{s}_{linear}(x,y) = \frac{\pi}{2}\begin{bmatrix} 0 & 1 & 2 & 3 \end{bmatrix}. \tag{2.5}$$

Chronologically, the 2×2 stacked configuration was the first one to be presented [2, 21]; next comes the 2×2 circular configuration [3, 12, 31]; and finally there is the more recently proposed 1×4 linear configuration [20, 32]. It may be proved that all other 4-step possibilities are related to these configurations merely by rotations or reflections, so they do not produce different results. As it will be shown in the following sections, these unit-cells are the basis of operation for conventional phase-demodulation methods, and the spectral behavior or this technique also depends on the unit-cell.

2.2 Conventional phase-shifting algorithms demodulation

Since the non-linear 2D pixelated carrier $c(x,y)$ is assumed to be known, a straightforward method to demodulate $\varphi(x,y)$ is to rearrange the information in $I(x,y)$ according to the phase-step observed in each pixel to generate four "conventional" phase-shifted interfero-

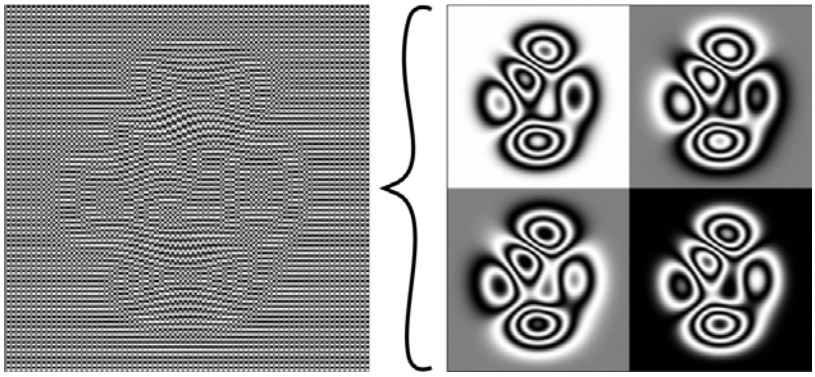

Figure 2.2: Low-resolution simulation, for ease of observation, of a pixelated phase-shifted interferogram (left-side, with a 256×256 pixels resolution) being rearranged to produce four "conventional" phase-shifted interferograms (right-side, each one with a 128×128 pixels resolution).

grams as follows: $[(2x,2y) \rightarrow (\xi,\eta)]$

$$\begin{aligned}
I_0(\xi,\eta) &= a(\xi,\eta)+b(\xi,\eta)\cos[\varphi(\xi,\eta)]\,,\\
I_1(\xi,\eta) &= a(\xi+1,\eta)+b(\xi+1,\eta)\cos[\varphi(\xi+1,\eta)+\pi/2]\,,\\
I_2(\xi,\eta) &= a(\xi+1,\eta+1)+b(\xi+1,\eta+1)\cos[\varphi(\xi+1,\eta+1)+\pi]\,,\\
I_3(\xi,\eta) &= a(\xi,\eta+1)+b(\xi,\eta+1)\cos[\varphi(\xi,\eta+1)+3\pi/2]\,. \qquad (2.6)
\end{aligned}$$

The change of variable in the spatial dependency of the left-side was made to highlight the fact that these "conventional" phase-shifted interferograms do not have the same resolution as the original $I(x,y)$, but rather a quarter of it (see Fig. 2.2). Assuming that the functions $\{a(x,y),b(x,y),\varphi(x,y)\}$ do not vary significantly whiting a 2×2 neighborhood, it is possible to apply the following approximations:

$$a(\xi,\eta) \approx a(\xi+1,\eta) \approx a(\xi,\eta+1) \approx a(\xi+1,\eta+1), \qquad (2.7)$$

$$b(\xi,\eta) \approx b(\xi+1,\eta) \approx b(\xi,\eta+1) \approx b(\xi+1,\eta+1), \qquad (2.8)$$

$$\varphi(\xi,\eta) \approx \varphi(\xi+1,\eta) \approx \varphi(\xi,\eta+1) \approx \varphi(\xi+1,\eta+1). \qquad (2.9)$$

Substituting these approximations in Eq. 2.6, results:

$$\begin{aligned}
I_0(\xi,\eta) &= a(\xi,\eta)+b(\xi,\eta)\cos[\varphi(\xi,\eta)]\,,\\
I_1(\xi,\eta) &= a(\xi,\eta)+b(\xi,\eta)\cos[\varphi(\xi,\eta)+\pi/2]\,,\\
I_2(\xi,\eta) &= a(\xi,\eta)+b(\xi,\eta)\cos[\varphi(\xi,\eta)+\pi]\,,\\
I_3(\xi,\eta) &= a(\xi,\eta)+b(\xi,\eta)\cos[\varphi(\xi,\eta)+3\pi/2]\,. \qquad (2.10)
\end{aligned}$$

Then, the searched phase map is simply computed (modulo 2π) as the angle of the following analytic signal:

$$A_0(\xi,\eta)\exp[i\hat{\varphi}(\xi,\eta)] = I_0(\xi,\eta) - iI_1(\xi,\eta) - I_2(\xi,\eta) + iI_3(\xi,\eta)\,. \tag{2.11}$$

Thus, in its simplest possible interpretation, the pixelated phase-mask technique is a high-tech solution to encode several phase-steps into a single image-shot. However, this demodulation approach requires information rearrange, which increases the computation time, and the estimated phase has a *quarter* of the original spatial resolution. Moreover, this demodulation method also introduces significant detuning-errors for phase maps under study with fast spatial-changes inside the unit-cell [12, 31, 32]; i.e. whenever the approximations in Eq. 2.9 are invalid. Said detuning-errors translate into a double-frequency spurious term in the output signal (as it is illustrated in Fig. 2.3). Thus, the applicability of this method must be restricted (in principle) to phase-maps with low spatial-frequency.

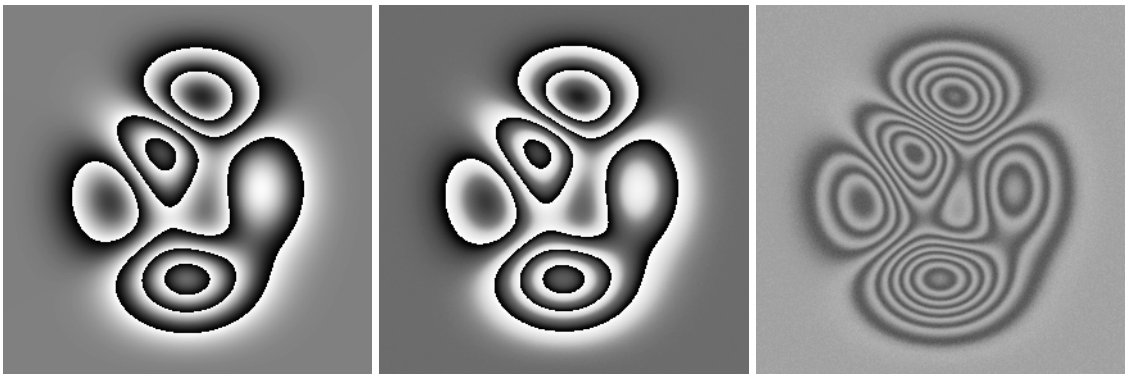

(a) (b) (c)

Figure 2.3: Assessment of the conventional phase-shifting algorithms demodulation. In this simulation we used our standard 512×512 pixels resolution for the pixelated phase-shifted interferogram, which means that these results have a 256×256 pixels resolution. Panel (a) shows the ideally expected result $\varphi(\xi,\eta)$. Panel (b) shows the estimated phase $\hat{\varphi}(\xi,\eta)$ as obtained from Eq. 2.11. Panel (c) shows the wrapped difference between $\varphi(\xi,\eta)$ and $\hat{\varphi}(\xi,\eta)$; the contrast in this result was digitally enhanced for ease of observation.

2.3 Fourier transform demodulation

In 2012 Servin et al. [32] proposed another demodulation method for pixelated phase-shifted interferograms that relies in information rearrange. The main idea in this method is

to take the 2D pixelated carrier interferogram, given by

$$I(x,y) = a(x,y) + b(x,y)\cos[\varphi(x,y) + c(x,y)], \tag{2.12}$$

and transform it into a linear carrier interferogram. For instance, one may produce the quarter-resolution phase-shifted interferograms discussed in the previous section, $\{I_n(\xi,\eta)\}$ for $n = \{0,1,2,3\}$, and rearrange their information into a single interferogram by doing the following operations:

$$\begin{aligned} I'(4\xi,\eta) &= I_0(\xi,\eta;0), \\ I'(4\xi+1,\eta) &= I_1(\xi,\eta;\pi/2), \\ I'(4\xi+2,\eta) &= I_2(\xi,\eta;\pi), \\ I'(4\xi+3,\eta) &= I_3(\xi,\eta;3\pi/2). \end{aligned} \tag{2.13}$$

The result is a linear carrier interferogram stretched in the horizontal-axis direction,

$$I'(4\xi,\eta) = a(4\xi,\eta) + b(4\xi,\eta)\cos[\varphi(4\xi,\eta) + u_0\xi], \quad (u_0 = \pi/2). \tag{2.14}$$

This open-fringes interferogram can be demodulated with the Fourier method as follows:

$$A_0(4\xi,\eta)\exp[i\hat{\varphi}(4\xi,\eta)] = LPF\{I'(4\xi,\eta)\exp(-iu_0\xi)\}. \tag{2.15}$$

Should be noted that the resulting demodulated phase $\hat{\varphi}(4\xi,\eta)$ is stretched four times in the $x-$direction. Thus, the last step of this demodulation technique is a backward mapping, the squeezing process, to return the estimated phase to the quarter-resolution space (ξ,η). An illustrative example of this demodulation method is shown in Fig. 2.4

Clearly, for this method it is also assumed that the functions $\{a,b,\varphi\}$ do not vary significantly withing a 2×2 neighborhood (as in the temporal phase-shifting demodulation approach). However, it is well-known that the Fourier demodulation technique is much more robust against detuning-error since one completely wipes-out the spectral region of the unwanted components instead of narrow stop-band regions as is done with few-steps phase-shifting algorithms [11, 32, 33, 37]. On the downside, this method requires slightly more computation time than the conventional phase-shifting algorithms demodulation and (as will be shown in the following section) its spectral behavior is not optimal.

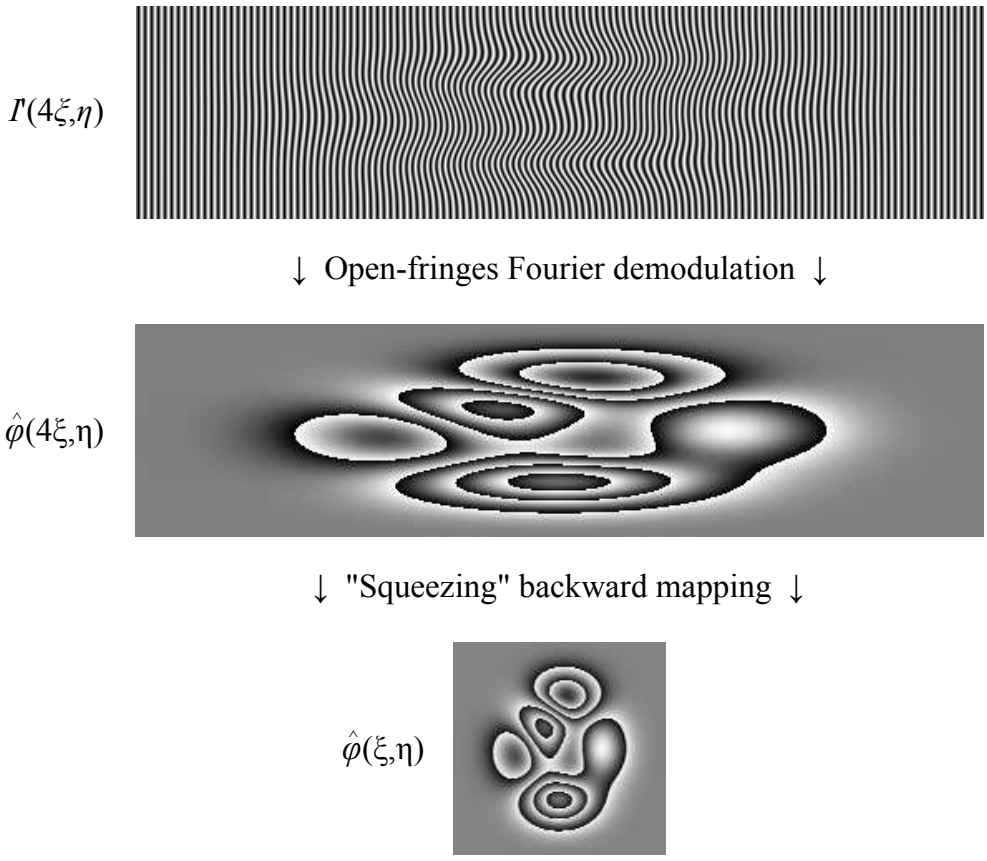

Figure 2.4: Illustrative example of the squeezing interferometry technique. The four steps in the 512×512 pixelated phase-shifted interferogram are rearranged according to Eq. 2.13 to produce an open-fringes pattern $I'(4\xi,\eta)$, having a 1024×256 pixels resolution. This high-frequency, open-fringes pattern is phase-demodulated with the Fourier method. Since the estimated phase $\hat{\varphi}(4\xi,\eta)$ is horizontally stretched, the final step is a squeezing process to correct the horizontal proportion. The final result lies within the 256×256 pixels resolution space (ξ,η); that is, it has only a quarter of the original resolution (just as in the temporal approach discussed in Section 2.2).

2.4 Pixelated carrier synchronous demodulation

Briefly after proposing the Fourier transform demodulation for pixelated phase-shifted interferograms, Servin and Estrada [31] proposed a much more convenient approach that consist in just two steps: the first one is to take the synchronous product between the original pixelated phase-shifted interferogram,

$$I(x,y) = a(x,y) + b(x,y)\cos[\varphi(x,y) + c(x,y)], \tag{2.16}$$

and the 2D pixelated carrier $\exp[-ic(x,y)]$:

$$I(x,y,t)\exp[-ic(x,y)] = a(x,y)\exp[-ic(x,y)] + (1/2)b(x,y)\exp[i\varphi(x,y)] + (1/2)b(x,y)\exp\{-i[\varphi(x,y)+2c(x,y)]\}. \quad (2.17)$$

Since the frequency of the 2D pixelated carrier is (in principle) much higher than the frequency of the searched phase, then the only low-frequency signal in the above equation is given by the searched analytic signal $(1/2)b(x,y)\exp[i\varphi(x,y)]$. The next and final step is simply to apply a real-valued low-pass filter (LPF) to this synchronous product[1]:

$$LPF\{I(x,y)\exp[-ic(x,y,t)]\} = (1/2)b(x,y)\exp[i\hat{\varphi}(x,y)]. \quad (2.18)$$

Once again, the searched modulated phase $\hat{\varphi}(x,y)$ can be straightforwardly computed (modulo 2π) as the angle of this analytic signal, and the local contrast function $b(x,y)$ is proportional to its magnitude. Should be noted that this synchronous demodulation approach has the following advantages respect to the conventional methods previously analyzed in this chapter:

1. **Improved computation time since it does not require information rearranging.**
2. **Detuning-error robustness thanks to the broad stop-band filtering in the spatial frequency domain.**
3. **The estimated phase has the same resolution as the original pixelated phase-shifted interferogram.**

An illustrative example is shown in Fig. 2.5 for the stacked configuration (the circular configuration *looks* identical and the linear configuration is simply a high-frequency open-fringes interferogram).

[1] It is preferably to apply the low-pass filtering in the Fourier domain for more robustness, although spatial convolution with averaging masks is also a valid possibility. This will be discussed in detail in chapter 3.

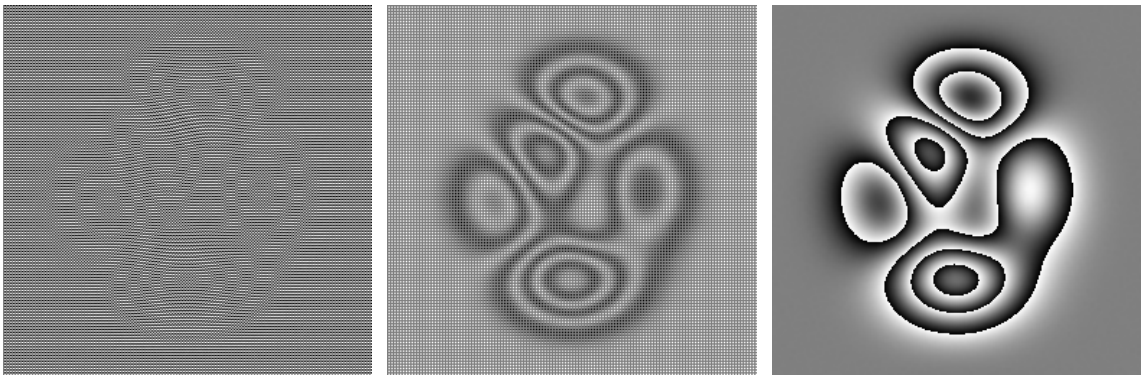

(a) (b) (c)

Figure 2.5: Illustrative example of the synchronous demodulation for pixelated phase-shifted interferograms. Panel (a) shows the pixelated phase-shifted interferogram $I(x,y)$ as seen in the CCD camera. Panel (b) shows the real part of the synchronous product $I(x,y,t)\exp[-ic(x,y)]$. Panel (c) shows the wrapped estimated phase $\hat{\varphi}(x,y)$ as obtained from the angle of the analytic signal $LPF\{I(x,y)\exp[-ic(x,y,t)]\}$.

2.4.1 Analysis in the spatial Fourier domain

As we reported in [26], it is possible to model a pixelated phase-mask as:

$$\begin{aligned}\exp[i\mathbf{s}(x,y)] &= \delta(x,y)+e^{i\pi/2}\delta(x-1,y)+e^{i\pi}\delta(x,y-1)+e^{i3\pi/2}\delta(x-1,y-1),\\ \exp[ic(x,y)] &= \exp[i\mathbf{s}(x,y)]**\sum_m\sum_n\delta(x-2m,y-2n),\end{aligned} \tag{2.19}$$

where we are assuming a 2×2 circular configuration for the unit-cell or "super-pixel" $\mathbf{s}(x,y)$. Alternatively, in the Fourier domain we have for the pixelated carrier [26]:

$$W_k(u,v)=\mathscr{F}\{\exp[ik\mathbf{s}(x,y)]\},\quad \text{for}\quad k=\{1,2\}, \tag{2.20}$$

$$\mathscr{F}\{\exp[ikc(x,y)]\}=\sum_m\sum_n W_k(m\pi,n\pi)\delta(u-m\pi,v-n\pi). \tag{2.21}$$

Substituting in the Fourier transform of the synchronous product $\mathscr{F}\{I(x,y)\exp[-ic(x,y)]\}$ (see Eq. 2.17), it can be probed that the Fourier transform of the searched analytic signal, $\mathscr{F}\{(1/2)b(x,y)\exp[-i\varphi(x,y)]\}$, remains at the base-band; while the spectral lobes $\mathscr{F}\{a(x,y)\}$ and $\mathscr{F}\{(1/2)b(x,y)\exp[-i\varphi(x,y)]\}$ are replicated at the spectral frequencies $(m\pi,n\pi)$ and weighted by the numerical values $W_k(m\pi,n\pi)$, for $k=\{1,2\}$ and $\{m,n\}=\{\pm1,\pm2,...\}$. This analytic analysis for the spectral behavior of the synchronous demodulation method can be confusing and cumbersome but, on the other hand, its numerical assessment is rather straightforward.

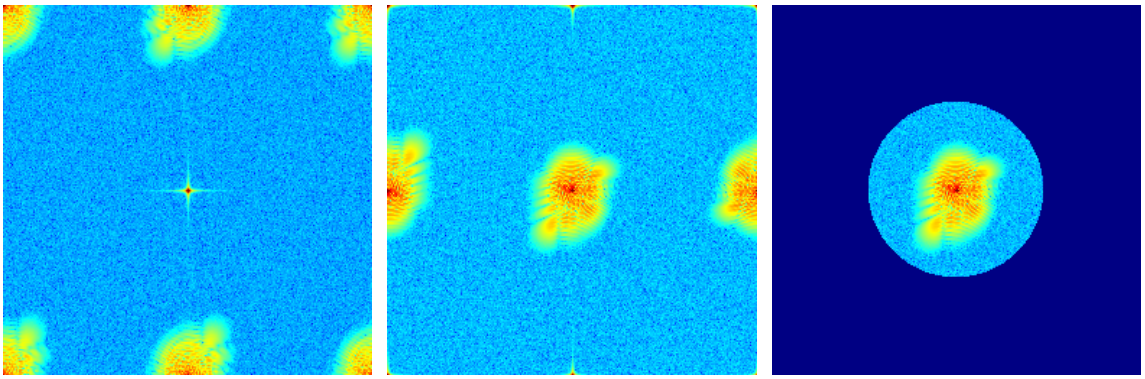

(a) (b) (c)

Figure 2.6: Synchronous demodulation of a PPS interferogram with "stacked" configuration. Panel (a) shows the Fourier spectra of $I(x,y)$. Panel (b) shows the spectral distribution of the synchronous product $I(x,y)\exp[-ic(x,y)]$. Panel (c) shows the searched spectral lobe $\mathscr{F}\{(1/2)b(x,y)\exp[i\varphi(x,y)]\}$ isolated at the base-band after linear filtering.

Next are shown several numerical simulations to illustrate and assess the synchronous demodulation method for 4-steps pixelated phase-shifted interferograms (see Fig. 2.6-2.8). For ease of observation, these are low-resolution simulations (256×256 pixels) so the spectral lobes would appear rather large even for the low-frequency signals being used. Nevertheless, the actual resolution of the pixelated phase-mask in commercially available solutions is up-to 6 megapixels[2], which means that these low-frequency signals would fit in a much smaller region of the spectral domain.

The first case to be analyzed (see Fig. 2.6) is the 2×2 "stacked" configuration, where the unit-cell or super-pixel is given by:

$$\mathbf{s}_{stacked}(x,y) = \frac{\pi}{2}\begin{bmatrix} 0 & 1 \\ 2 & 3 \end{bmatrix}. \tag{2.22}$$

Panel 2.6(a) shows that the pixelated carrier modulation produces a significant spectral separation between the spectral lobes. Panel 2.6(b) shows how the synchronous product $I(x,y)\exp[-ic(x,y)]$ sends the spectral $\mathscr{F}\{(1/2)b(x,y)\exp[i\varphi(x,y)]\}$ to the base-band while its conjugate complex lies π radians away. This means that the maximum spatial frequency in the fringe pattern that can be demodulated with this configuration without distortion due to spectral overlap is just below of $(\pi/2)$ radians per pixel.

[2]http://www.4dtechnology.com/products/index.php, Retrieved in 2014-02-15.

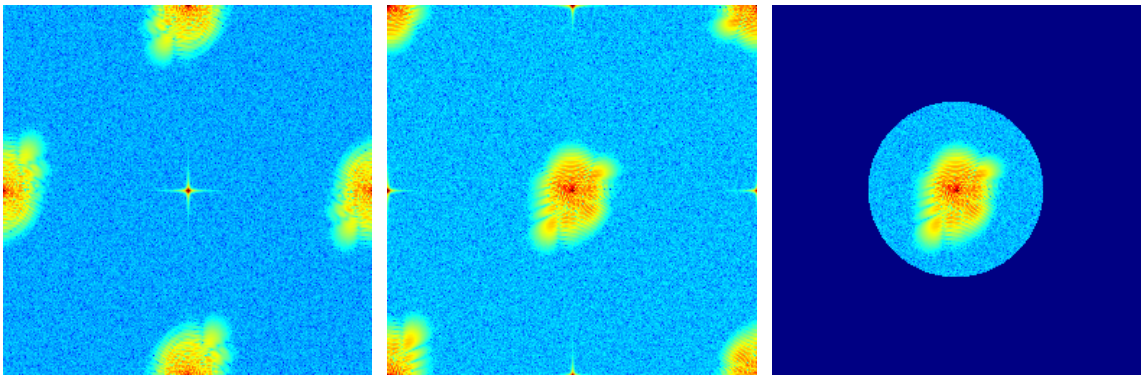

(a) (b) (c)

Figure 2.7: Synchronous demodulation of a pixelated phase-shifted interferogram with "circular" configuration. Panel (a) shows the Fourier spectra of $I(x,y)$. Panel (b) shows the spectral distribution of the synchronous product $I(x,y)\exp[-ic(x,y)]$. Panel (c) shows the searched spectral lobe $\mathscr{F}\{(1/2)b(x,y)\exp[i\varphi(x,y)]\}$ isolated at the base-band after linear filtering.

The next case to be analyzed (see Fig. 2.7) is the 2×2 "circular" configuration, where the unit-cell or super-pixel is given by [3, 12, 31]:

$$\mathbf{s}_{circular}(x,y) = \frac{\pi}{2}\begin{bmatrix} 0 & 1 \\ 3 & 2 \end{bmatrix}. \tag{2.23}$$

By comparison between Panel 2.6(b) and Panel 2.7(b), we can see that the spectral separation between the searched spectral lobe $\mathscr{F}\{(1/2)b(x,y)\exp[i\varphi(x,y)]\}$ and its conjugate complex is greater for the circular configuration $(\sqrt{2}\pi)$ than for the staked configuration (π). Thus, the maximum spatial frequency in the fringe pattern that can be demodulated with this configuration without distortion due to spectral overlap is just below of $(\pi/\sqrt{2})$ radians per pixel. This means that the "circular" configuration makes a better use of the spectral domain in comparison with the "staked" configuration, despite the fact that the only difference between them is the physical distribution of the phase-steps.

The final 4-step pixelated carrier to be analyzed is the 1×4 linear configuration (see Fig 2.8), where the unit-cell or super-pixel is given by [20, 32]:

$$\mathbf{s}_{linear}(x,y) = \frac{\pi}{2}\begin{bmatrix} 0 & 1 & 2 & 3 \end{bmatrix}. \tag{2.24}$$

This is the most recently proposed 4-step unit-cell configuration and, according to Millerd et al. [20], this is the less complex PPM to align with the CCD camera. Unfortunately, this is also the 4-step configuration with the lest efficient use of the spectral domain [32].

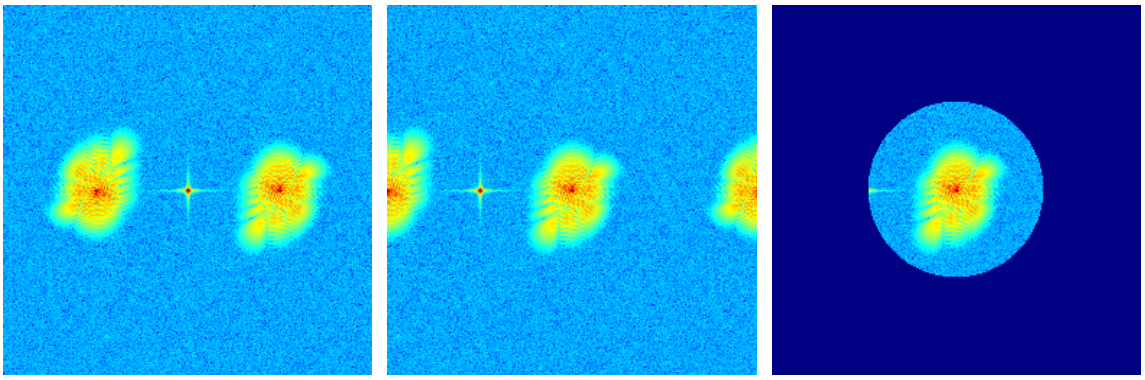

(a) (b) (c)

Figure 2.8: Synchronous demodulation of a pixelated phase-shifted interferogram with linear configuration. Panel (a) shows the Fourier spectra of $I(x,y)$. Panel (b) shows the spectral distribution of the synchronous product $I(x,y)\exp[-ic(x,y)]$. Panel (c) shows the searched spectral lobe $\mathscr{F}\{(1/2)b(x,y)\exp[i\varphi(x,y)]\}$ isolated at the base-band after linear filtering.

As we can see from Panel 2.8(b), the 1×4 linear configuration produces a spectral separation of π radians between the searched spectral lobe $\mathscr{F}\{(b/2)\exp(i\varphi)\}$ and its conjugate complex; that is as good as the separation achieved with the stacked configuration but lower than those of the circular configuration ($\sqrt{2}\pi$ radians). Moreover, as we can see from Panel 2.8(c), the maximum spatial frequency in the fringe pattern that can be demodulated without spectral overlap is just below $(\pi/2)$ radians per pixel but in this case the background signal $\mathscr{F}\{a(x,y)\}$ may also introduce aberrations, instead of just the conjugate complex $\mathscr{F}\{(b/2)\exp(-i\varphi)\}$ as in the previously analyzed 2×2 configurations.

To summarize

Synchronous demodulation is the easiest, yet more convenient and efficient method to demodulate pixelated phase-shifted interferograms. And even when its spectral behavior is more complex to describe because the 2D pixelated carrier $c(x,y)$ cannot be modeled (in general) by a linear function, numerical simulations show that the 2×2 "circular" configuration makes the better use of the spectral domain for 4-step pixelated phase-masks.

Chapter 3

Analysis of systematic errors

In the previous chapter we analyzed the spectral behavior of the synchronous demodulation method for pixelated phase-shifted interferograms *when working under ideal conditions*. Now we are ready to discuss the most commonly observed systematic errors: additive white-Gaussian noise, detuning error and high-order distorting harmonics. This will allow us to propose novel configurations and hybrid methods to improve the robustness of this technique.

3.1 Additive noise in PPS interferometry

In fringe pattern analysis we deal with two kinds of noise: additive noise, which comes from the ambient and the electronic equipment used; and speckle noise, observed when testing optically rough surfaces. However, when working with the synchronous demodulation method for pixelated phase-shifted interferograms, the spatial low-pass filtering modifies the statistical properties of the multiplicative noise into additive Gaussian noise. The theoretical foundation for this change in the statistical properties is the central limit theorem of stochastic (random) processes [27]. For our purposes, this theorem says that the output signal resulting from the linear filtering of a stochastic process with finite mean and variance tends to Gaussian statistics, no matter which statistical distribution the input process had. This means that, whether having additive noise and/or speckle noise, the low-pass filtering will turn the output noise "more Gaussian and additive". Thus, our mathematical model for a noisy pixelated phase-shifted interferogram will be given simply by:

$$I(x,y) = a(x,y) + b(x,y)\cos[\varphi(x,y) + c(x,y)] + n_a(x,y)\,, \tag{3.1}$$

where $a(x,y)$ is the background signal, $b(x,y)$ is the local contrast function, $\varphi(x,y)$ is phase-map under study and $c(x,y)$ is the 2D pixelated carrier. In the pessimistic (or cautious) approach, the noise term $n_a(x,y)$ is assumed to be an uncorrelated stochastic signal with flat power spectral density (psd) $N_a(u,v) = \eta/2$ –that is with equal contribution within any frequency bands– and Gaussian amplitude distribution of variance σ^2: in order words, we assume an additive white-Gaussian noise (AWGN).

As demonstrated in the previous chapter, the most convenient demodulation method for pixelated phase-shifted interferograms consists in low-pass filtering the synchronous product $I(x,y)\exp[-ic(x,y)]$:

$$\begin{aligned} S(x,y) &= \{I(x,y)\exp[-ic(x,y)]\} ** h(x,y) \\ &= (1/2)b(x,y)\exp[i\hat{\varphi}(x,y)] + \{n_a(x,y)\exp[-ic(x,y)]\} ** h(x,y)\,, \end{aligned} \tag{3.2}$$

where ** represents the 2D convolution operation and $h(x,y)$ is the input response function of a real-valued low-pass filter. It can be proved[1] that the expectation value for $S(x,y)$ is given by the searched analytic signal,

$$E[S] = (1/2)b(x,y)\exp[i\hat{\varphi}(x,y)], \tag{3.3}$$

while its standard deviation is due exclusively to the filtered additive noise,

$$N(u,v) = \mathscr{F}\{n_a(x,y)\exp[-ic(x,y)]\}, \tag{3.4}$$

$$E[S^2] = \sigma_S^2 = \frac{1}{(2\pi)^2}\iint_{-\pi}^{\pi} |N(u,v)|^2 |H(u,v)|^2 du dv\,. \tag{3.5}$$

Moreover, since the input noise's psd is assumed to be uniform, we can also assume that the psd for the complex-valued noise $n_a(x,y)\exp[-ic(x,y)]$ is given by $N(u,v) = \eta/2$ despite the spectral displacement due to the synchronous product. Thus, we have:

$$\sigma_S^2 = \frac{\eta}{8\pi^2}\iint_{-\pi}^{\pi} |H(u,v)|^2 du dv\,. \tag{3.6}$$

In short: the expectation value is still the searched analytical signal, $(b/2)\exp(i\hat{\varphi})$, while the amount of complex-valued noise in the output signal depends on the power spectral density of the input signal's noise ($\eta/2$) and the absolute square of the low-pass filter's frequency transfer function, $|H(u,v)|^2$.

[1] For a detailed analysis, although from a temporal quadrature linear filtering perspective, see [34].

Up-to this point the assumed that it is possible to apply a binary mask to low-pass filter in the Fourier domain since (in principle) this allows us to reject as much noise as possible without over-filtering the searched analytic signal at the base-band. However, in our experience this approach requires considerably more computation time than a simple 2D convolution product with averaging masks.

As demonstrated in the previous chapter, we need a low-pass filter whose frequency transfer function fulfills the conditions $H(m\pi, n\pi) = 0$ for $\{m,n\} = \{\pm 1, \pm 2, ...\}$. The following is a list of valid averaging masks for the low-pass filtering of 2×2 unit-cell configurations[2]:

$$
\begin{aligned}
h_1(x,y) &= \frac{1}{4}\begin{bmatrix} 1 & 1 \\ 1 & 1 \end{bmatrix}, \\
h_2(x,y) &= \frac{1}{4^2}\begin{bmatrix} 1 & 2 & 1 \\ 2 & 4 & 2 \\ 1 & 2 & 1 \end{bmatrix} = h_1(x,y) * * h_1(x,y), \\
h_3(x,y) &= \frac{1}{4^3}\begin{bmatrix} 1 & 3 & 3 & 1 \\ 3 & 9 & 9 & 3 \\ 3 & 9 & 9 & 3 \\ 1 & 3 & 3 & 1 \end{bmatrix} = h_1(x,y) * * h_1(x,y) * * h_1(x,y), \\
&\vdots \\
h_n(x,y) &= (4^{-n})\{h_1(x,y) * * h_1(x,y)\}^n, \qquad (3.7)
\end{aligned}
$$

where $\{h_1(x,y) * * h_1(x,y)\}^n$ means taking the 2D self-convolution product n times. The frequency transfer function for these averaging mask is shown in Fig. 3.1. These results are congruent with the averaging kernels proposed by Novak et al. [23] and Kimbrough and Millerd [14].

[2]Note that pixelated phase-mask configurations with unit-cells of different size (1×4, 2×3, 3×3 and so on) will require different averaging masks.

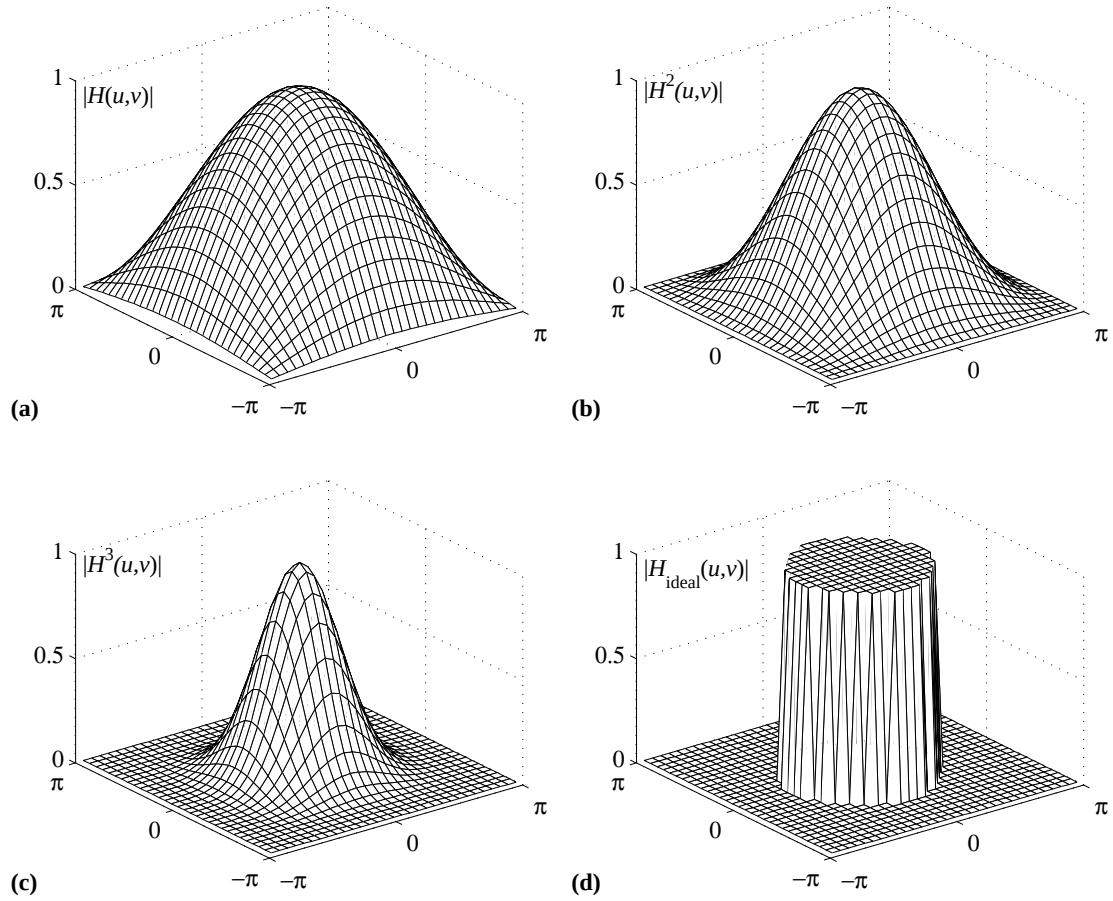

Figure 3.1: (a-c) Frequency transfer function, $|H^{k+1}(u,v)|$ for $k = \{0,1,2\}$ where k indicates the number of convolutions with the 2×2 basic averaging mask (see Eq. 3.7), and (d) the ideal mask-based Fourier filter for reference.

3.2 Detuning-error in PPS interferometry

Quite probably the most common systematic error in temporal phase-shifting interferometry, the detuning-error arises when the synchronous demodulation is tuned to work with a given phase-step ω_0 but the interferometric data actually has a phase-step carrier $\omega_0 + \Delta$, being some unknown value in radians per sample [33]. However, unlike temporal phase-shifting interferometry where Δ is usually uniform (i.e., a fixed value for the entire image-plane), in pixelated phase-shifting interferograms we have a particular phase-step for each pixel, so it is logical to define an spatially dependent error-function $\varepsilon(x,y)$ instead. This means that our mathematical model for a pixelated phase-shifted interferogram with

detuning-error will be given by:

$$I(x,y) = a(x,y) + b(x,y)\cos[\varphi(x,y) + c(x,y) + \varepsilon(x,y)]\,. \tag{3.8}$$

Proceeding with the synchronous demodulation as usual, one straightforwardly finds:

$$LPF\{I(x,y)\exp[-ic(x,y)]\} = (1/2)b(x,y)\exp\{i[\hat{\varphi}(x,y) + \varepsilon(x,y)]\}\,. \tag{3.9}$$

That is, the detuning-error in pixelated phase-shifted interferometry produces a high frequency spurious contribution to the estimated phase. In practice, one expects this detuning-error to be relatively low due to quality control in the manufacturing process, but high precision measurements require that residual errors in the interferometric system are minimized [13, 23].

Assuming that the error-function $\varepsilon(x,y)$ remains stationary, we can either use a known test subject or we can determine $\varphi(x,y)$ from alternative means; for instance, we can use a high-precision optical flat or temporal phase-shifting techniques [13]. Given a known $\varphi(x,y)$ we can solve Eq. 3.9 for (an estimated) detuning-error function $\hat{\varepsilon}(x,y)$ in order to "recalibrate" the pixelated phase-mask:

$$LPF\{I(x,y)\exp[-ic(x,y)]\} \times \exp[-i\hat{\varepsilon}(x,y)] = (1/2)b(x,y)\exp[i\hat{\varphi}(x,y)]\,. \tag{3.10}$$

Note that we chose not to combine $c(x,y)$ and $\hat{\varepsilon}(x,y)$ into a single demodulation carrier $c'(x,y) = c(x,y) + \hat{\varepsilon}(x,y)$, because $c(x,y)$ is a least-squares solution (with phase-step values given by $2\pi/N$, with $N = 4$). This means that the demodulation method will be more robust against additive noise and (as we will demonstrate in the following section) to high-order distorting harmonics if we keep demodulating the pixelated carrier interferogram using $c(x,y)$ instead of $c'(x,y)$. Thus, what we gain by performing this calibration process is the attenuation of the high-frequency residual error in the estimated phase (Eq. 3.10). A numerical simulation to assess this compensation/calibration approach is shown in Fig. 3.2, where we assume a significant error-field $\hat{\varepsilon}(x,y) \in (-\pi/8, \pi/8)$ for illustrative purposes.

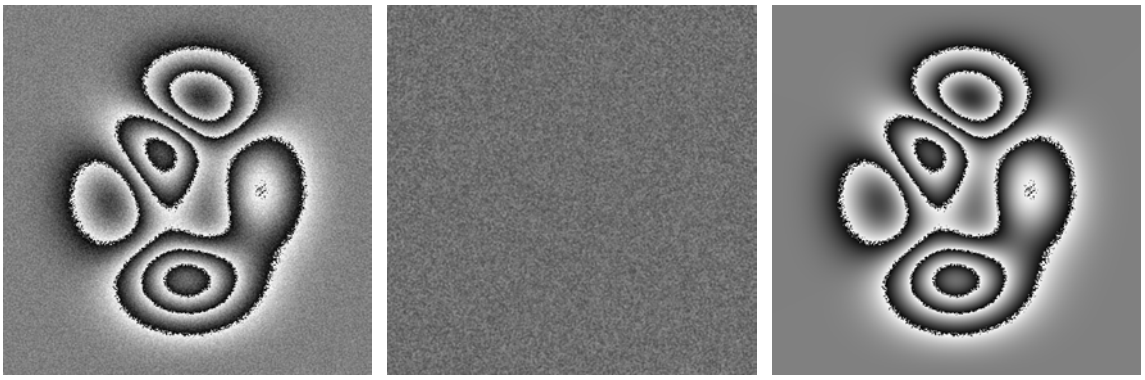

(a) (b) (c)

Figure 3.2: Numerical simulation to assess the impact of detuning-error in pixelated phase-shifted interferometry. Panel (a) shows the erroneously demodulated phase $\hat{\varphi}(x,y) + \varepsilon(x,y)$. Panel (b) shows the stationary error-field $\hat{\varepsilon}(x,y)$ estimated with a known test subject (with enhanced contrast for ease of observation). Finally, panel (c) shows the properly demodulated $\hat{\varphi}(x,y)$ after the proposed calibration process.

Should be noted that this recalibration process would be required, in principle, just once for each pixelated phase-mask. After that, the entire interferometric system is ready to work with fast-changing dynamic phenomena as usual. For an alternative method to cope with this kind on residual phase-errors, see for instance [13, 23] and its references.

3.3 Distorting harmonics in PPS interferometry

When designing or assessing demodulation methods it is usually assumed at first approximation that our interferometric fringes have a perfect sinusoidal profile. However, in practice we often deal with non-sinusoidal fringe patterns due to gain saturation (non-linear photodetector response), multiple beams interferences, and so on. These systematic errors lead to the generation of high-order harmonics of the fundamental signal which degrades the quality of the estimated phase [33, 34]. A useful mathematical model for pixelated phase-shifted interferogram with non-sinusoidal fringes is given by the following Fourier expansion [24, 25]:

$$I(x,y) = (1/2) \sum_{k=-\infty}^{\infty} b_k(x,y) \exp\{ik[\varphi(x,y) + c(x,y)]\}, \tag{3.11}$$

where $b_0(x,y) \approx a(x,y)$ is the background signal, $b_k(x,y) \in \mathbb{C}^2$ are the contrast function for the $k-$th harmonic, and all other terms remain as previously defined. Following the synchronous demodulation method, the first step it to take the product $I(x,y)\exp[-ic(x,y)]$,

given by [24, 25]:

$$I(x,y)\exp[-ic(x,y)] = (1/2)\sum_{k=-\infty}^{\infty} b_k(x,y)\exp[ik\varphi(x,y)]\exp[i(k-1)c(x,y)]\,,$$
$$= b_0\exp(-ic) + (b_1/2)[\exp(i\varphi) + \exp(-i\varphi)\exp(-i2c)] + \ldots \quad (3.12)$$

The first terms of the summation were shown to illustrate the similarity with the ideally expected result (Eq. 2.17). Thanks to the symmetry of the 2D pixelated carrier $c(x,y)$ we are able to deduce especial cases for $\exp[i(k-1)c(x,y)]$ by working explicitly over their fundamental unit-cell $\mathbf{s}(x,y)$ as follows [24] (notice that here we are using the 2×2 circular configuration)

$$\exp[\pm i\mathbf{s}(x,y)] = \exp\left[\pm i\begin{pmatrix} 0 & \pi/2 \\ 3\pi/2 & \pi \end{pmatrix}\right] \Rightarrow \exp[\pm ic(x,y)], \quad (3.13)$$

$$\exp[\pm 2i\mathbf{s}(x,y)] = \exp\left[\pm 2i\begin{pmatrix} 0 & \pi \\ \pi & 2\pi \end{pmatrix}\right] \Rightarrow \exp[\pm i\pi(x+y)], \quad (3.14)$$

$$\exp[\pm 3i\mathbf{s}(x,y)] = \exp\left[\pm 3i\begin{pmatrix} 0 & 3\pi/2 \\ \pi/2 & \pi \end{pmatrix}\right] \Rightarrow \exp[\pm ic(x,y)^T], \quad (3.15)$$

$$\exp[\pm 4i\mathbf{s}(x,y)] = \exp\left[\pm 4i\begin{pmatrix} 0 & 2\pi \\ 6\pi & 4\pi \end{pmatrix}\right] = \begin{bmatrix} 1 & 1 \\ 1 & 1 \end{bmatrix}. \quad (3.16)$$

Clearly, for distorting harmonics of fifth order and above, the respective carrier will be identical to one of the above listed possibilities. Substituting in Eq. 3.12 and grouping the terms with the same pixelated carrier, results [24]:

$$I(x,y)\exp(-ic) = (1/2)\{b_1\exp(i\varphi) + b_3\exp(-i3\varphi) + b_5\exp(i5\varphi) + b_7\exp(-i7\varphi) + \ldots\}$$
$$+ (1/2)\{b_1\exp(-i\varphi) + b_3\exp(i3\varphi) + b_5\exp(-i5\varphi) + \ldots\}\exp[i\pi(x+y)]$$
$$+ \{b_0 + b_2\cos(2\varphi) + b_4\cos(4\varphi) + b_6\cos(6\varphi) + \ldots\}\exp(ic^T)\,. \quad (3.17)$$

Note that the terms in the first row do not undergo any spectral shift; they are all located at the base-band along with $b_1\exp(i\varphi)$. The terms in the second row, multiplied by $\exp[i\pi(x+y)]$, are displaced to the spectral corners $(u,v) = (\pm\pi, \mp\pi)$. Finally, the terms in the third row are shifted by the transpose of the 2D carrier to the cardinal points $(u,v) = (0, \pm\pi)$ and $(u,v) = (\pm\pi, 0)$. Thus, applying the appropriate low-pass filter $h(x,y)$, the terms in the

second and third row are suppressed [24]:

$$A_0(x,y)\exp[i\hat{\varphi}(x,y)] = \{I(x,y)\exp[-ic(x,y)]\} * *h(x,y)\,, \tag{3.18}$$
$$= b_1\exp[i\varphi(x,y)] + \sum_{k=1}^{\infty} b_{2k+1}\exp[i(-1)^k(2n+1)\varphi(x,y)]\,,$$

where $A_0(x,y)$ is proportional to the fringes' local contrast function. This result was reported in [24], which as far as we know was the first ever harmonics analysis for spatial synchronous demodulation of pixelated phase-shifted interferograms.

For illustrative purposes, we show in Fig. 3.3-3.4 several stages of the demodulation process for a pixelated phase-shifted interferogram having non-sinusoidal closed-fringes. As demonstrated in the previous chapter, the more efficient use of the spectral domain is achieved with the 2×2 unit-cell "circular" configuration; thus only this case will be analyzed here. For this numerical simulation we used a mixture of low mean level (64 bits for a 0-255 range) and introduced gain saturation in order to generate high-energy distorting harmonics. Also note that in order to have a less complex Fourier spectrum, henceforward we will use a simpler fringe pattern [24].

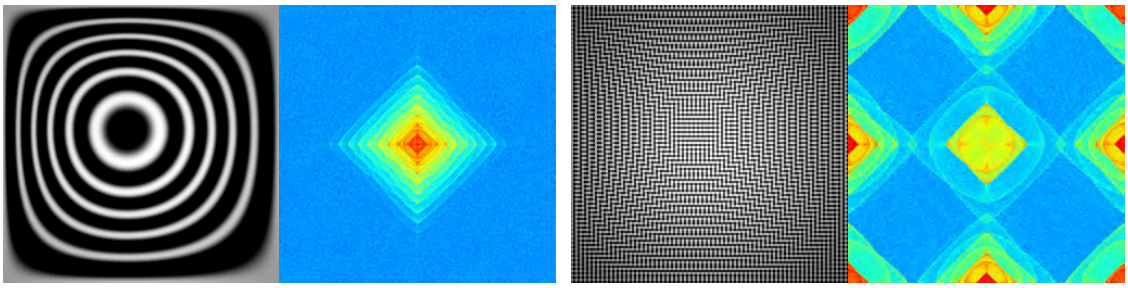

(a) (b)

Figure 3.3: Panel (a) shows a non-sinusoidal closed-fringes pattern having several harmonics overlapped at the spectral origin. Panel (b) shows the pixelated phase-shifted interferogram as would be observed in the CCD camera with identical conditions as the ones that produce the non-sinusoidal fringes in panel (a).

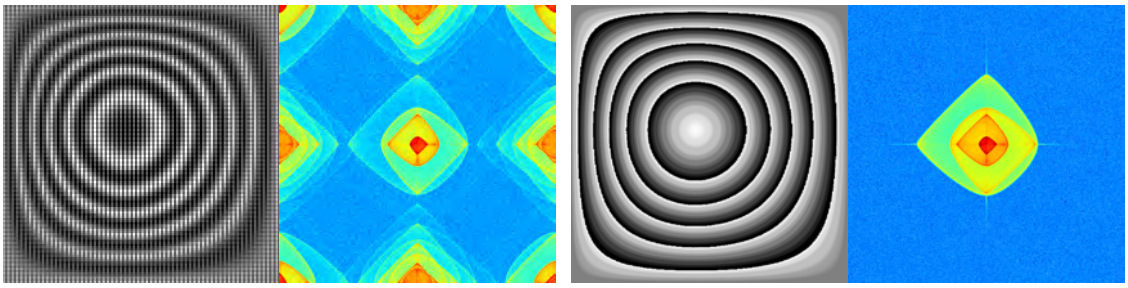

(a) (b)

Figure 3.4: Panel (a) shows the real part of the synchronous product $I(x,y)\exp[-ic(x,y)]$ for the non-sinusoidal closed-fringes pattern, and its Fourier spectrum. Panel (b) shows the wrapped phase with distorting harmonics distortion; as predicted by the theory, the $\{-3^{\text{rd}}, 5^{\text{th}}, -7^{\text{th}}\}$ distorting harmonics are clearly identifiable in the spectral domain.

From the numerical simulation in Fig. 3.3-3.4, and according with our heuristic mathematical analysis, we conclude that the output analytic signal for this harmonically distorted pixelated phase-shifted interferogram will be given in general by:

$$LPF\{I(x,y)e^{-ic(x,y)}\} = \frac{1}{2}\{b_1 e^{i\varphi} + b_3 e^{-i3\varphi} + b_5 e^{i5\varphi} + b_7 e^{-i7\varphi} + \ldots\}. \tag{3.19}$$

For the trained eye in temporal phase-shifting interferometry it is clear that the $\{-3,+5,-7\}$ distorting harmonics are precisely the ones observed when a 4-step least-squared phase-shifting algorithm (LS-PSA) is applied (see Fig. 3.5). This result is to be expected since both approaches used the same number of phase-shifted samples, $N = 4$, and the same phase-step value $\omega_0 = 2\pi/4$. Nevertheless, as illustrated in panel 3.4(b) and Fig. 3.6, this harmonics rejection capability is not enough to achieve high-quality phase estimations from these non-sinusoidal fringes patterns [24].

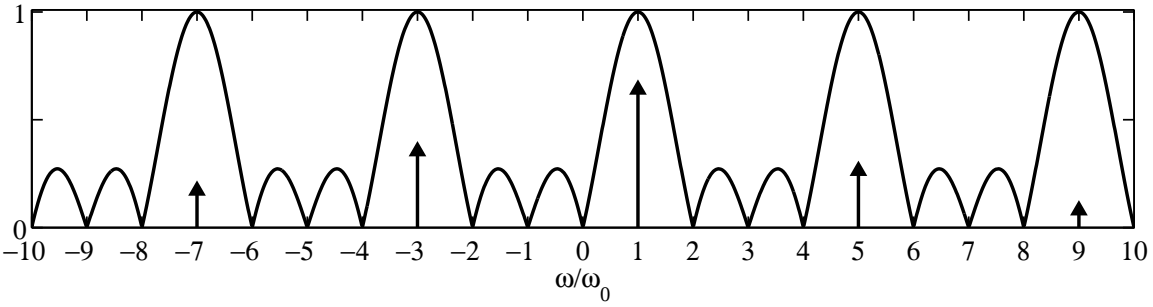

Figure 3.5: Normalized-frequency harmonics response, $|H(\omega)|$ versus ω/ω_0, for the 4-step least-squares phase-shifting algorithm, where $\omega_0 = 2\pi/4$. For more references, see [4, 34].

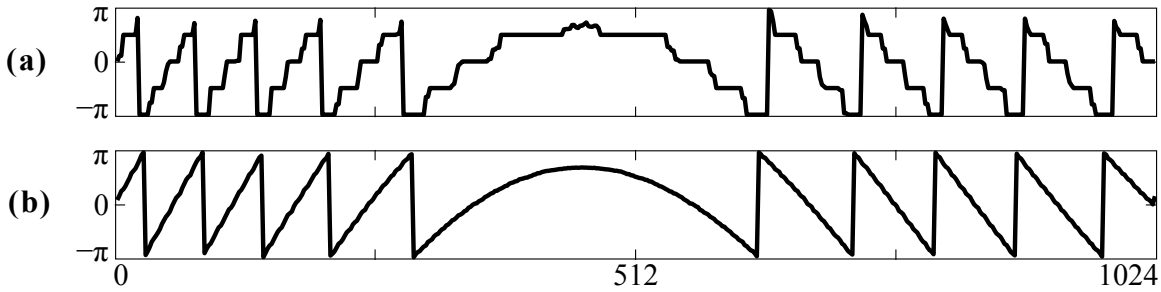

Figure 3.6: Qualitative comparison between the estimated phase from the 2×2 unit-cell pixelated phase-shifted interferogram (a), versus the ideally expected result (b). Both plots have the same resolution; the stepped variations in panel (a) are due exclusively to high-frequency distorting harmonics.

To summarize:

In this chapter were analyzed the most commonly observed systematic errors and its implications for the synchronous demodulation of pixelated phase-shift interferometry.

For additive white-Gaussian noise (AWGN) it was shown that the amount of complex-valued noise in the output signal depends on the power spectral density of the input signal's noise ($\eta/2$) and the absolute square of the low-pass filter's frequency transfer function $|H(u,v)|^2$. It was also showed a general formula for valid averaging masks to be used in high performance low-pass filtering for 2×2 unit-cell configurations.

For the detuning-error in pixelated phase-shifting interferometry we showed that it results into a high-frequency contribution to the output estimated phase –on the form $\hat{\varphi}(x,y) = \varphi(x,y) + \varepsilon(x,y)$– and we proposed a straightforward algorithmic approach to cope with this contribution during the calibration process.

Finally we showed that the synchronous demodulation of pixelated phase-shifted interferograms has identical harmonics-rejection capabilities as the 4-step LS-PSA, which is the theoretical maximum for the given number of phase-shifted samples. In the following chapter will be discussed two approaches to enhance the harmonics rejection capabilities of this technique: increasing the number of the phase-shifted samples and spatio-temporal phase demodulation.

Chapter 4

Novel configurations and hybrid methods

In the previous chapter we presented the Fourier analysis of the most commonly observed systematic errors and its influence for the synchronous demodulation of pixelated phase-shifted interferograms. We already discussed two possibilities to improve the robustness of this technique against additive white-Gaussian noise and detuning-error; and now we will show two alternatives to cope with high-order distorting harmonics: a novel configuration for the pixelated phase-mask and spatio-temporal synchronous demodulation. The ability to reject high-order harmonics is very important in fringe pattern analysis because their presence in the output signal degrades the quality of the estimated phase.

4.1 Increasing the phase-shifted samples

Previously we demonstrated that it is possible to achieve the harmonics rejection capabilities of a 4-step least-squares phase-shifting algorithm (LS-PSA) with the synchronous demodulation of a 2×2 unit-cell pixelated phase-shifted (PPS) interferogram. If we want to improve this harmonic rejection capability, an educated guess is that the spectral behavior of higher-order LS-PSAs can be matched by increasing the number of phase-shifted samples within the unit-cell. To test this asseveration we analyzed several pixelated phase-mask (PPMs) with alternative configurations using 2×3, 2×4 and 3×3 unit-cells, which naturally allow encoding $N = \{6, 8, 9\}$ phase-steps (in each case we used $\omega_0 = 2\pi/N$). We found that 2×3 unit-cell configurations make the better use of the spectral domain –although not as efficiently as 2×2 unit-cell configurations– but changing from 4 to 6

phase-steps does not increase considerably the harmonic rejection capability of this technique. On the other hand, using a 3×3 unit-cell configuration means a good compromise between encoding many phase-steps and making a good use of the spectral domain. From the tested configurations we concluded that the 3×3 "spiral" unit-cell configuration (see Fig. 4.1) produces the most efficient spectral behavior; nevertheless, if this is *the* most spectrally efficient 3×3 configuration, it is yet an open question.

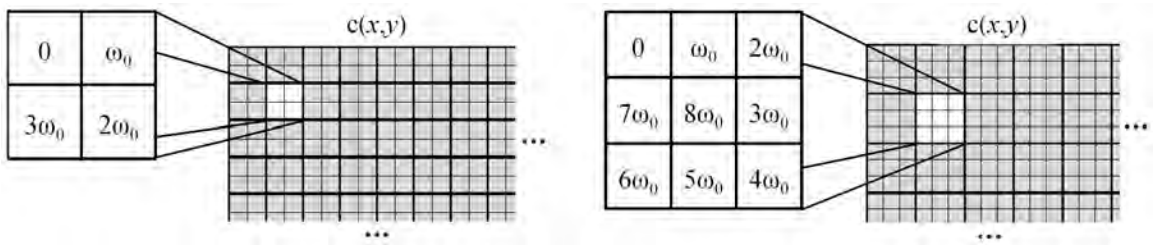

Figure 4.1: Schematic comparison of (4-steps) 2×2 "circular" and (9-steps) 3×3 "spiral" unit-cells for pixelated phase-shifting interferometry.

As it was demonstrated in Chapter 2, the spectral behavior of the pixelated carrier modulation is ruled by the phase-step distribution within the unit-cell [26], which for our proposed 3×3 "spiral" unit-cell configuration it is given by: ($\omega_0 = 2\pi/9$)

$$\begin{aligned}\exp[i\mathbf{s}(x,y)] = [\,&\delta(x,y) + e^{i\omega_0}\delta(x-1,y) + e^{i2\omega_0}\delta(x-2,y) \\ &+ e^{i7\omega_0}\delta(x,y-1) + e^{i8\omega_0}\delta(x-1,y-1) + e^{i3\omega_0}\delta(x-2,y-1) \\ &+ e^{i6\omega_0}\delta(x,y-2) + e^{i5\omega_0}\delta(x-1,y-2) + e^{i4\omega_0}\delta(x-2,y-2)]\,, \\ \exp[ic(x,y)] = \exp[i\mathbf{s}(x,y)] &** \sum_m \sum_n \delta(x-3m, y-3n)\,. \end{aligned} \tag{4.1}$$

Proceeding as we did for the analysis of 2×2 unit-cell configurations, the first step is to enter this information in our mathematical model for a pixelated phase-shifted interferogram with non-sinusoidal fringes, given by:

$$I(x,y) = (1/2) \sum_{k=-\infty}^{\infty} b_k(x,y) \exp\{ik[\varphi(x,y) + c(x,y)]\}\,, \tag{4.2}$$

where $b_0(x,y)$ is the background signal, $b_k(x,y)$ are the contrast function for the $k-$th fringe-pattern harmonic, $\varphi(x,y)$ is the modulating phase under study, and $c(x,y)$ is the 2D pixelated carrier. The second step for the synchronous demodulation method is to calculate

the synchronous product $I(x,y)\exp[-ic(x,y)]$, given by [24, 25]:

$$I(x,y)\exp[-ic(x,y)] = (1/2)\sum_{k=-\infty}^{\infty} b_k(x,y)\exp[ik\varphi(x,y)]\exp[i(k-1)c(x,y)]\,. \qquad (4.3)$$

Particularly we need to analyze the harmonics of the pixelated carrier in the Fourier domain, $\mathscr{F}\{\exp[ikc(x,y)]\}$ for $k=\{1,2,...\}$, in order to identify which distorting harmonics remain at the spectral origin overlapping with the searched analytic signal $(b_1/2)\exp(i\varphi)$. That is:

$$W_k(u,v) = \mathscr{F}\{\exp[ik\mathbf{s}(x,y)]\}, \quad \text{for} \quad k=\{1,2,...\}, \qquad (4.4)$$

$$\mathscr{F}\{\exp[ikc(x,y)]\} \;=\; \sum_m\sum_n W_k\left(m\frac{2\pi}{3}, n\frac{2\pi}{3}\right)\delta\left(u-m\frac{2\pi}{3}, v-n\frac{2\pi}{3}\right). \qquad (4.5)$$

Substituting in the Fourier transform of the synchronous product, $\mathscr{F}\{I(x,y)\exp[-ic(x,y)]\}$ (see Eq. 4.2), it can be probed that not only the searched analytic signal remains at the base-band but also its {-8th, +10th, ...} distorting harmonics. Thus, after applying the proper low-pass filtering, the output signal for the synchronous demodulation of a (9-step) 3×3 "spiral" configuration pixelated phase-shifted interferogram will be given by [25, 26]:

$$LPF\{I(x,y)\exp[-ic(x,y)]\} = \frac{1}{2}\{b_1 e^{i\varphi} + b_8 e^{-i8\varphi} + b_{10}e^{i10\varphi} + \ldots\} \approx \frac{b_1}{2}e^{i\varphi}\,, \qquad (4.6)$$

where the last approximation is supported by the fact that $(b_{10} < b_8) \ll b_1$. Moreover, from Eq. 4.5 we also know that the maximum spatial frequency in the searched phase that can be demodulated without spectral overlap will be $\pi/3$ radians. These conclusions are confirmed by our numerical simulations: note in Fig. 4.2 that the {-8th,+10th,...} distorting harmonics are barely discernible from the Fourier transform of the synchronous product, $\mathscr{F}\{I(x,y)\exp[-ic(x,y)]\}$, despite the fact that these spectral plots are displayed in logarithmic intensity scale.

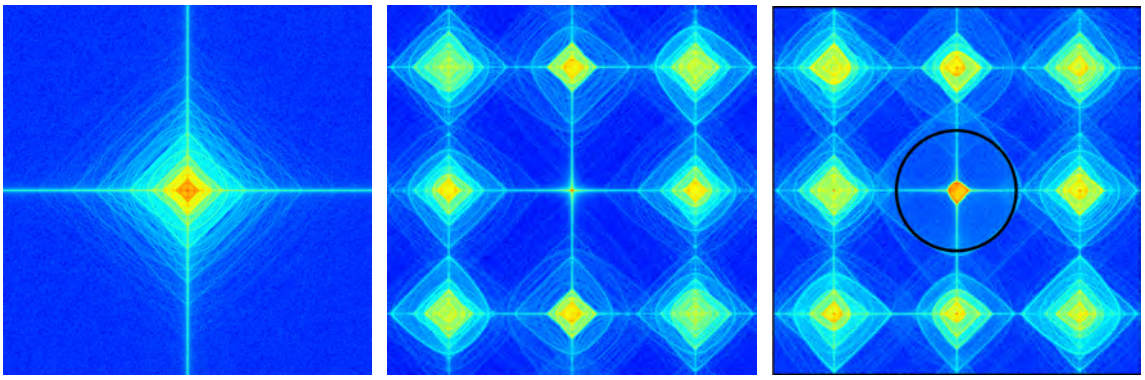

(a) (b) (c)

Figure 4.2: Several stages of the demodulation process for a 9-step pixelated phase-shifted interferogram with 3×3 spiral configuration and non-sinusoidal closed-fringes. Panel (a) shows $\mathscr{F}\{I(x,y)\}$ without any carrier showing all the harmonics overlapping at the base-band. Panel (b) shows the spectral redistribution due to the 2D pixelated carrier; that is the Fourier transform of Eq. 4.2. Panel (c) shows $\mathscr{F}\{I(x,y)\exp[-ic(x,y)]\}$, where the dark ring of radio $\pi/3$ indicates the maximum spatial frequency in the searched phase that can be demodulated without spectral overlap.

Analyzing Eq. 4.6 and Fig. 4.2, it is clear that the 3×3 "spiral" configuration translates into a harmonics-rejection capability more a robust than those of the 2×2 configurations previously tested, and equivalent to that of the 9-step LS-PSA (see Fig. 4.3).

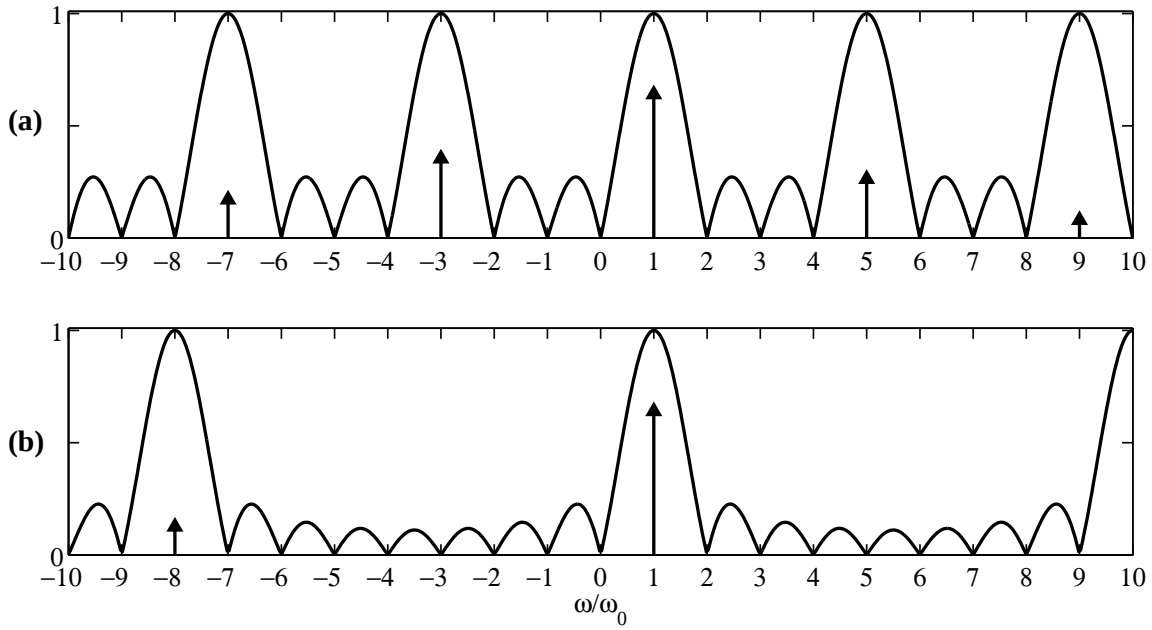

Figure 4.3: Normalized-frequency harmonics response, $|H(\omega)|$ versus ω/ω_0, for (a) the 4-step and (b) the 9-step LS-PSAs. For more references, see [4, 34].

From Eq. 4.5, we know that the phase-demodulation of a pixelated phase-shifted interferogram with this 3×3 "spiral" configuration requires a low-pass filter whose FTF satisfies at least the conditions $H(2m\pi/3,2n\pi/3)=0$ for $\{m,n\}=\{\pm1,\pm2,...\}$. To this end, the most robust approach is to use a binary-mask filtering in the Fourier domain; which for this case means to reject all components of $\mathscr{F}\{I(x,y)\exp[-ic(x,y)]\}$ that fall outside a disk of ratio $\pi/3$, centered at the spectral origin. However, this approach is usually much slower than a two-dimensional convolution product using averaging masks. Thus, whenever the phase demodulation of the PPM interferogram is required to be done on the fly, the fastest approach is given by:

$$LPF\{I(x,y)\exp[-ic(x,y)]\}=\{I(x,y)\exp[-ic(x,y)]\}**h(x,y)\,. \tag{4.7}$$

As Fig. 4.4 shows, the following is a list of valid averaging masks whose frequency transfer function fulfill the required spectral conditions $H(2m\pi/3,2n\pi/3)=0$ for $\{m,n\}=\{\pm1,\pm2,...\}$.

$$\begin{aligned}
h_1(x,y) &= \frac{1}{9}\begin{bmatrix}1&1&1\\1&1&1\\1&1&1\end{bmatrix},\\
h_2(x,y) &= \frac{1}{9^2}\begin{bmatrix}1&2&3&2&1\\2&4&6&4&2\\3&6&9&9&3\\2&4&6&4&2\\1&2&3&2&1\end{bmatrix}=h_1(x,y)**h_1(x,y)\,,\\
&\vdots\\
h_n(x,y) &= (9^{-n})\{h_1(x,y)**h_1(x,y)\}^n\,,
\end{aligned} \tag{4.8}$$

where $\{h_1(x,y)**h_1(x,y)\}^n$ means taking the 2D self-convolution product n times. Clearly these averaging masks are not new but, as far as we known, until now it was unknown which averaging masks are required for the low-pass filtering of 3×3 unit-cell pixelated phase-shifted interferograms.

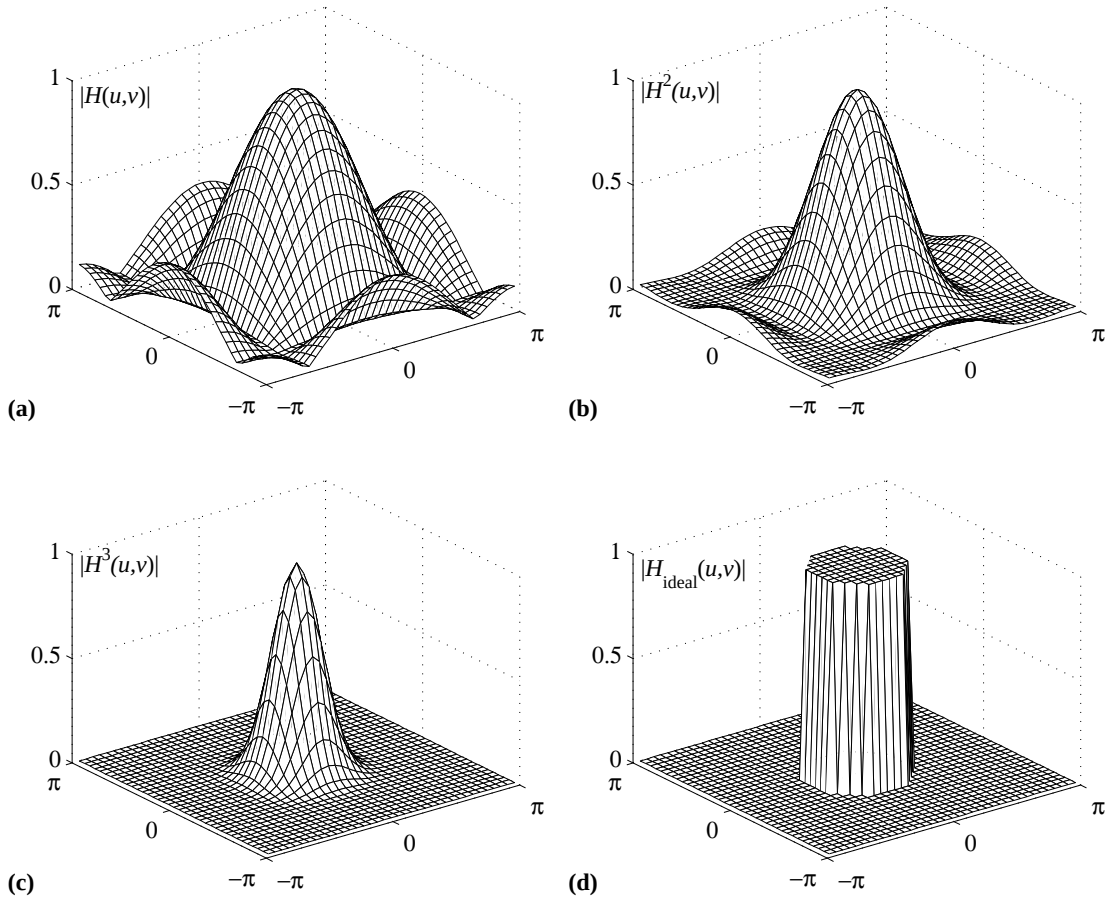

Figure 4.4: (a-c) Frequency transfer function, $|H^{k+1}(u,v)|$ for $k = \{0,1,2\}$ where k indicates the number of convolutions with the 3×3 basic averaging mask (see Eq. 4.8), and (d) the ideal binary filter's spectral response for reference.

In addition to comparing it with the commercially available 2x2 "circular" configuration, we believe that it is also interesting to compare the 3x3 "spiral" configuration against the same 9 steps distributed linearly; for this purpose we present Fig. 4.5 and 4.6. For this numerical simulation we generated three pixelated phase-shifted interferograms starting from the same non-sinusoidal fringe pattern which generates high-frequency distorting harmonics (just as in Panel 3.3(a)). The only difference between these simulations was the pixelated carrier modulation, using 2×2, 3×3 and 1×9 unit-cell configurations.

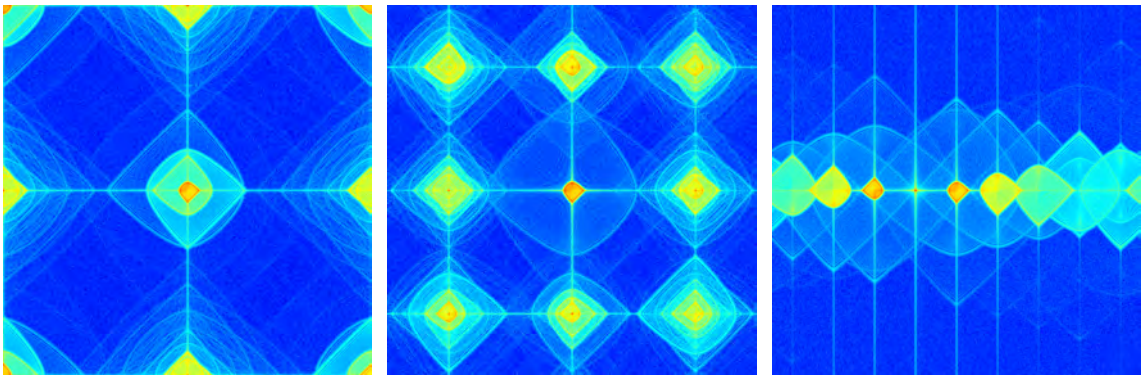

(a) (b) (c)

Figure 4.5: Fourier spectra of the complex-valued synchronous product $\{I(x,y)\exp[-ic(x,y)]\}$ for (a) 2×2, (b) 3×3 and (c) 1×9 unit-cell configurations of the pixelated phase-shift mask.

From Panels 4.5(a) and 4.5(b), it is clear that the separation among the spectral lobes decreases when the size of the unit-cell is increased; once again, this result was expected.

From panels 4.5(b) and 4.5(c) note that even when the same distorting harmonics are located at the base-band, the linear 1×9 unit-cell configuration makes a very inefficient use of the spectral domain, restricting the spatial frequency of the phase that can be demodulated to fulfill $|\nabla\varphi| < \pi/9$, whereas the 3×3 configuration would work for $|\nabla\varphi| < \pi/3$.

Also from Panels 4.5(b) and 4.5(c), we see that using the same 9-steps into a linear configuration results into a very tight spectral distribution of the high-order distorting harmonics around the spectral origin. Despite the fact that this linear configuration uses the same phase-step values as our proposed 3×3 "spiral" configuration, our educated guess is that this tight spectral distribution translates into more distorting harmonics energy in the output signal and, therefore, into a lower-quality estimated phase. This hypothesis was confirmed in our numerical simulations (see Fig. 4.6).

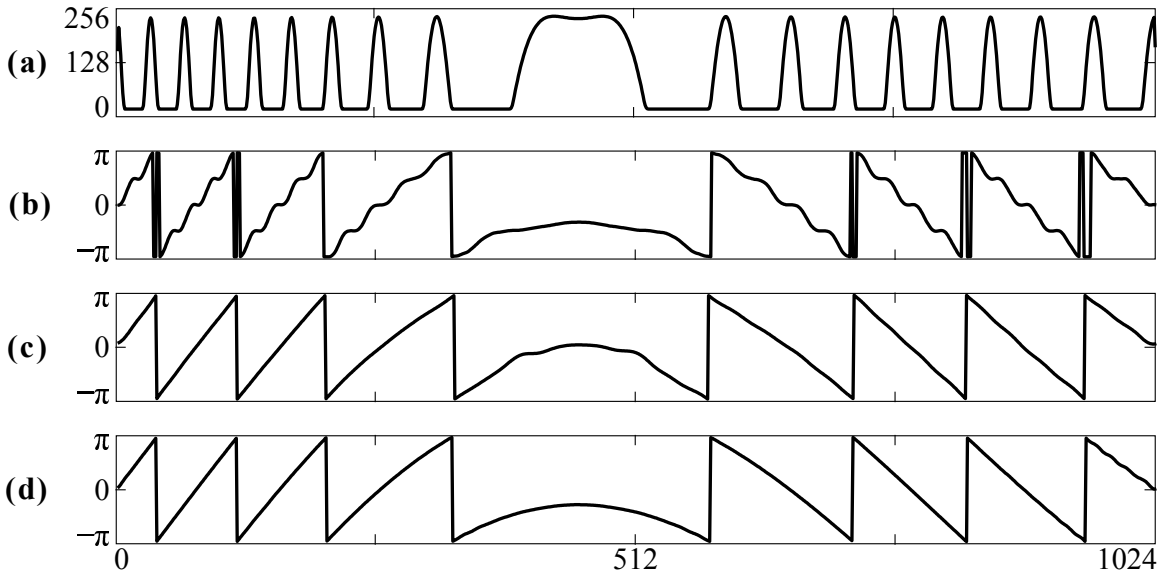

Figure 4.6: Horizontal slices for ease of observation of the harmonics-distorted pixelated phase-shifted interferogram being demodulated. Panel (a) shows amount of distortion on the closed-fringes pattern. Next panels show the estimated phase as obtained with: (b) 2×2 "circular", (c) 1×9 "linear" and (d) 3×3 "spiral" unit-cell configurations. The ideally expected result is visually indistinguishable from the estimated phase in panel (d).

Although all results in our numerical simulations were encouraging, the main disadvantage of this approach is that requires manufacturing a new and more complex type of pixelated phase-masks. For this reason we proposed a completely different approach easily achievable using the commercially available 2×2 unit-cell pixelated phase-masks: spatio-temporal demodulation with custom-made phase-shifting algorithms.

4.2 Spatio-temporal demodulation

In section 3.3 we analyzed pixelated phase-shifted interferograms with non-sinusoidal closed-fringes modulation, mathematically modeled by

$$I(x,y) = (1/2) \sum_{k=-\infty}^{\infty} b_k(x,y) \exp\{ik[\varphi(x,y) + c(x,y)]\}, \tag{4.9}$$

where $b_0(x,y)$ is the background signal, $b_k(x,y)$ are the contrast function for the $k-$th fringe-pattern harmonic, $\varphi(x,y)$ is the modulating phase under study, and $c(x,y)$ is the 2D pixelated carrier. As it was demonstrated in Eq. 3.18 (replicated here for the reader's convenience), the synchronous demodulation of this harmonically distorted pixelated phase-

shifted interferogram results in the following analytic signal [24]:

$$A_0(x,y)\exp[i\hat{\varphi}(x,y)] = \{I(x,y)\exp[-ic(x,y)]\} ** h(x,y)\,, \tag{4.10}$$
$$= b_1(x,y)\exp[i\varphi(x,y)] + \sum_{k=1}^{\infty} b_{2k+1}\exp[i(-1)^k(2n+1)\varphi(x,y)]\,.$$

That is, the output signal contains not just the searched signal $b_1(x,y)\exp[i\varphi(x,y)]$ but also its $\{-3,+5,-7,+9,...\}$ distorting harmonics, which must be rejected in order to obtain a high-quality phase estimation. Whenever it is possible, one may introduce a linear phase-step ω_0 between successive temporal samples of a distorted-fringes PPM interferogram,

$$I(x,y,t) = (1/2)\sum_{k=-\infty}^{\infty} b_k(x,y)\exp\{ik[\varphi(x,y)+c(x,y)+\omega_0 t]\}\,, \quad \{t=1,2,...\}. \tag{4.11}$$

Applying spatial synchronous demodulation to each temporal sample, the following analytic signal estimations are obtained: (note the subscript "1" indicating that the estimated phase was obtained from a single-image PPM interferogram)

$$\begin{aligned} A_0(x,y)\exp[i\hat{\varphi}_1(x,y)] &= b_1 e^{i\varphi} + b_3 e^{-i3\varphi} + b_5 e^{i5\varphi} + b_7 e^{-i7\varphi}... \\ A_0(x,y)\exp[i(\hat{\varphi}_1+\omega_0)] &= b_1 e^{i(\varphi+\omega_0)} + b_3 e^{-i3(\varphi+\omega_0)} + b_5 e^{i5(\varphi+\omega_0)} + ... \\ A_0(x,y)\exp[i(\hat{\varphi}_1+2\omega_0)] &= b_1 e^{i(\varphi+2\omega_0)} + b_3 e^{-i3(\varphi+2\omega_0)} + b_5 e^{i5(\varphi+2\omega_0)} + ... \end{aligned} \tag{4.12}$$

Alternatively, we may describe all these analytic signals, phase-shifted versions of Eq. 4.10, using a very compact notation as follows:

$$S(x,y,t) = \sum_{n=0}^{2} A_0(x,y)\exp\{i[\hat{\varphi}_1(x,y)+\omega_0 t]\}\delta(t-n)\,. \tag{4.13}$$

This signal still contains the complex-valued distorting harmonics $\{-3,5,-7,9,...\}$ that cannot be rejected via spatial synchronous demodulation since they overlap at the base-band with the searched analytic signal $(b_1/2)\exp(i\varphi)$; nevertheless, now we can use *temporal* quadrature linear filtering to reject them. For this purpose we propose the following 2-step phase-shifting algorithm (PSA) to reject the -3^{rd} and 5^{th} complex harmonics [24, 34]:

$$\begin{aligned} H_2(\omega) &= 1-\exp[i(\omega+3\omega_0)], \\ h_2(t) = \mathscr{F}^{-1}[H_2(\omega)] &= \delta(t) - e^{i3\omega_0}\delta(t+1); \quad \omega_0 = \pi/4\,. \end{aligned} \tag{4.14}$$

Similarly, the following 3-step PSA was designed to reject the -3^{rd},5^{th},-7^{th} and 9^{th} complex harmonics [24, 34]:

$$\begin{aligned} H_3(\omega) &= \Big\{1-\exp[i(\omega+3\omega_0)]\Big\}\Big\{1-\exp[i(\omega-5\omega_0)]\Big\}, \\ h_3(t) &= \delta(t)+[1-e^{i\omega_0}]\delta(t+1)+e^{i2\omega_0}\delta(t+2); \quad \omega_0=\pi/3\,. \end{aligned} \tag{4.15}$$

The normalized-frequency harmonics rejections capabilities of these custom-made PSAs are shown in Fig. 4.7. The continuous-line plots represent the FTF of the 2-step and 3-step temporal phase-shifted algorithms; $|H(\omega)|$. The crosses in the horizontal line represent the distorting harmonics that can be rejected with spatial synchronous demodulation and the vertical arrows represent the remaining components; the tallest Dirac delta at $\omega/\omega_0=1$ is the searched analytic signal $(b_1/2)\exp(i\varphi)$.

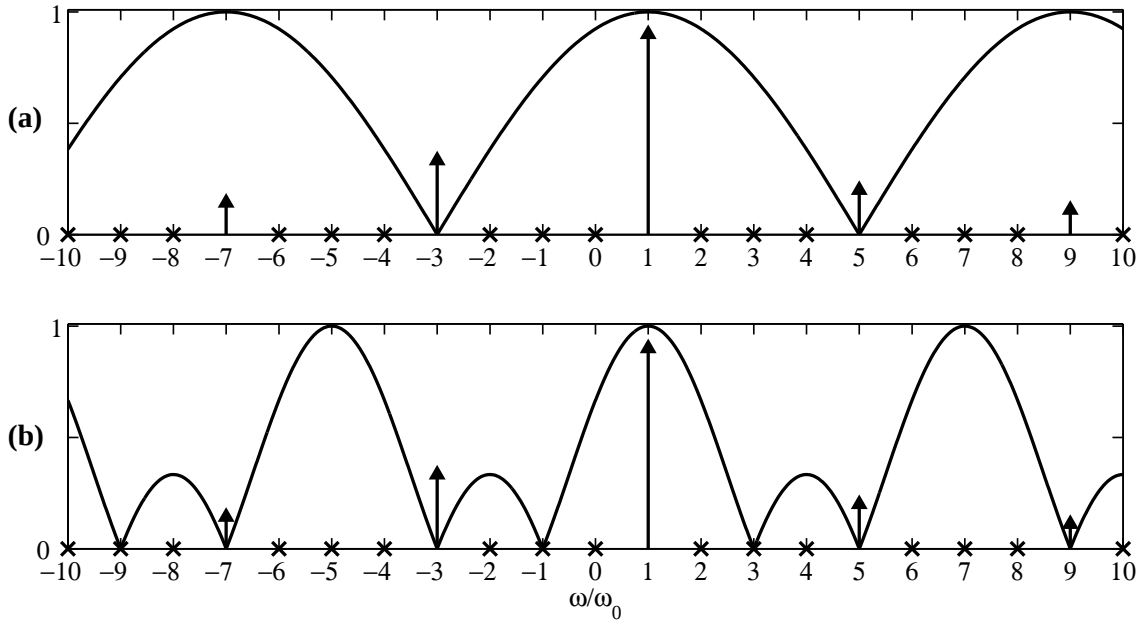

Figure 4.7: Harmonics rejection capabilities achieved with the spatio-temporal synchronous demodulation technique using a 2×2 unit-cell pixelated phase-masks in combination with (a) 2-step and (b) 3-step temporal PSAs. The elements of this figure are described in the text.

Applying the 2-step PSA from Eq. 4.14, the resulting analytic signal will be given by:

$$\begin{aligned} A_0(x,y)\exp[i\hat{\varphi}_2(x,y)] &= \{S(x,y,t)*h_2(t)\}_{t=2} = S_0(x,y)-e^{i3\omega_0}S_1(x,y)\,, \\ &= (1/2)\{b_1\exp(i\varphi)+b_7\exp(-i7\varphi)+b_9\exp(i9\varphi)+...\}\,, \end{aligned} \tag{4.16}$$

where $A_0(x,y)=(1/2)b(x,y)H_2(\omega_0)$ and $\omega_0=\pi/4$. Similarly, using the 3-step PSA from

Eq. 4.15, the resulting analytic signal will be given by:

$$\begin{aligned} A'_0(x,y)\exp[i\hat{\varphi}_3(x,y)] &= \{S(x,y,t)*h_3(t)\}_{t=3} = S_0(x,y)+[1-e^{i\omega_0}]S_1(x,y)+e^{i2\omega_0}S_2(x,y)\,, \\ &= (1/2)\{b_1\exp(i\varphi)+b_{11}\exp(-i11\varphi)+...\} \\ &\approx (1/2)b_1(x,y)\exp[i\varphi(x,y)]\,, \end{aligned} \tag{4.17}$$

where $A'_0(x,y) = (1/2)b(x,y)H_3(\omega_0)$ and $\omega_0 = \pi/3$. Note that up-to the tenth order, no distorting harmonics survive this 3-step spatio-temporal demodulation; this is illustrated in Panel 4.7(b). Also note that, in general, the distorting energy of very high-order harmonics will negligible**.** Finally, the most general expression for our spatio-temporal phase-demodulation algorithms is given by [24]:

$$A_0(x,y)\exp[i\hat{\varphi}_N(x,y)] = \Big(\{I(x,y,t)\exp[-ic(x,y)]**h(x,y)\}*h_N(t)\Big)_{t=N}\,, \tag{4.18}$$

being $h_N(t)$ an appropriate N-step quadrature linear filter[1]. This approach requires the computation of N synchronous products, N low-pass filtering processes and a single algebraic sum for the temporal quadrature linear filter; that is $(2N+1)$ full-image operations with $N = \{2,3,...\}$. Alternatively, if we exchange the implementation order of the spatial and temporal convolution, we have:

$$A_0(x,y)\exp[i\hat{\varphi}_N(x,y)] = \{\exp[-ic(x,y)][I(x,y,t)*h_N(t)]_{t=N}\}**h(x,y)\,. \tag{4.19}$$

In this approach, we require a single algebraic sum, a single synchronous product and a single low-pass filtering process; that is just three (instead of $2N+1$) full-image operations. Thus, we strongly recommend to use Eq. 4.19 for numerical efficiency [24].

For illustrative purposes, next in Fig. 4.8 and Fig. 4.9 we show the phase-demodulation of computer-simulated pixelated phase-shifted interferograms with non-sinusoidal closed-fringes using, respectively, conventional single-image demodulation (Eq. 4.10) and our custom-made 2-step and 3-step spatio-temporal algorithms (Eq. 4.16 and Eq. 4.17).

[1]While the 2-step and 3-step quadrature linear filters proposed in Eq. 4.16 and Eq. 4.17 provide optimal harmonic rejection capabilities, alternative filters may also be of interest. For instance, it is also possible to design a frequency transfer function with smooth spectral zeroes at $\omega/\omega_0 = \{-3,5\}$ in order to provide detuning robustness to the temporal filtering. For more details see [33, 34].

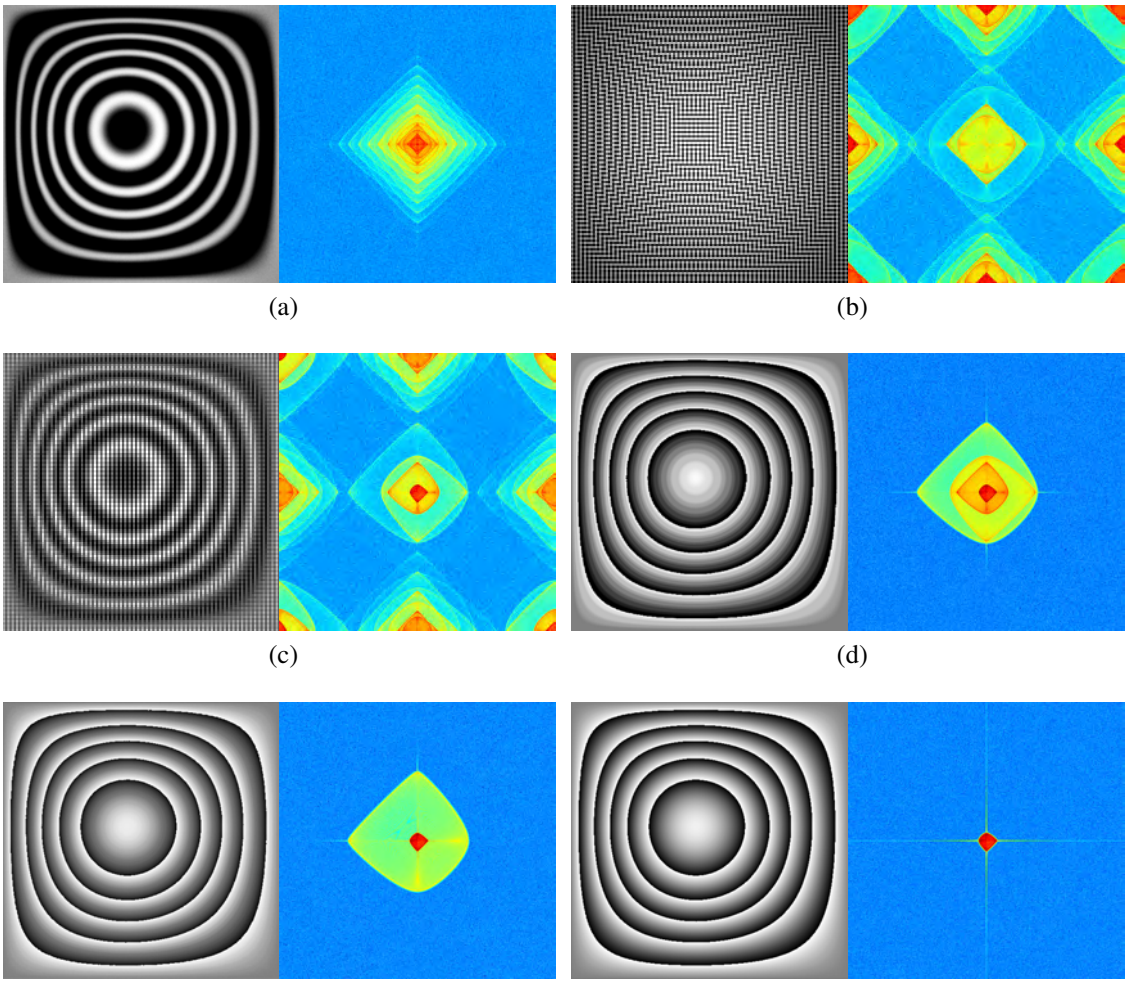

Figure 4.8: Several stages of the phase-demodulation of pixelated phase-shifted interferograms with high-order harmonic distortion. In each panel, the left-side corresponds to the spatial domain while the right-side shows the respective Fourier spectrum. Panel (a) shows a non-sinusoidal closed-fringes pattern having several harmonics overlapped at the spectral origin. Panel (b) shows the pixelated phase-shifted interferogram as would be observed in the CCD camera with identical conditions as the ones that produce the non-sinusoidal fringes in panel (a). Panel (c) shows the real part of the synchronous product $I(x,y)\exp[-ic(x,y)]$. Finally we have the wrapped-phases estimated with (d) single-image demodulation, (e) 2-step spatio-temporal demodulation, and (f) 3-step spatio-temporal demodulation.

From Panel 4.8(d) it is clear that the single-image estimated phase is distorted by its $\{-3^{\text{rd}}, 5^{\text{th}}, -7^{\text{th}}\}$ harmonics. From Panel 4.8(e), where the $\{-3^{\text{rd}}, 5^{\text{th}}\}$ harmonics were filter-out with the 2-step spatio-temporal algorithm, the output signal contains the searched analytic signal and its -7^{th} harmonic. Finally, from Panel 4.8(f) where our 3-step spatio-temporal algorithm was applied, no distorting harmonics are observed in the output signal.

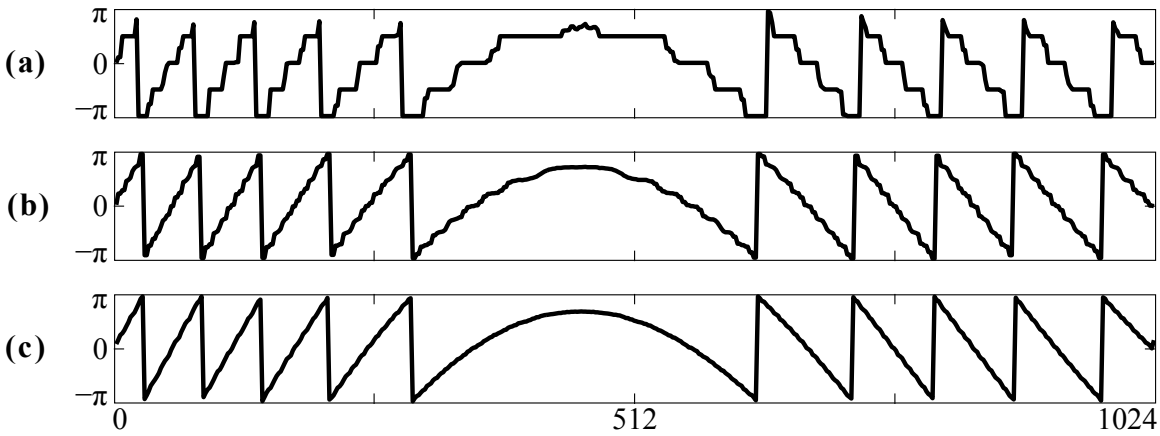

Figure 4.9: Horizontal slices of the estimated phase obtained from the 2D pixelated carrier interferogram with non-sinusoidal closed-fringes using (a) single-image demodulation, and the proposed (b) 2-step and (c) 3-step spatio-temporal algorithms.

For ease of observation, Fig. 4.9 shows horizontal slices of the estimated phases previously shown in Panels 4.8(d-f). The quality improvement with 2-step and 3-step demodulation is evident. This result proves that spatio-temporal demodulation is a useful approach to work with non-sinusoidal signals (a scenario which until this point was restricted to many-step phase-shifting algorithms). In other words, proper use of spatial and temporal phase-modulation relax the stability restrictions for the phenomenon under study by a factor of 4 while preserving the harmonics rejection robustness of a $4 \times N-$step LS-PSA.

To summarize:

We proposed and assessed alternative phase-mask configurations to improve the harmonics rejections capability of the pixelated phase-shifting demodulation technique. In particular, we found that a 3×3 unit-cell "spiral" configuration emulates the spectral behavior of the 9-step LS-PSA. Although the results of our numerical simulation were encouraging, the main disadvantage of this approach is that requires manufacturing a new (and more complex) type of pixelated phase-masks.

As alternative to the use of more complex PPM configurations, we demonstrated that few-steps temporal PSI techniques allow us to reject the distorting harmonics that remain at the base-band after the (single-image) spatial synchronous demodulation process is performed. We provide a general formula (Eq. 4.19) for the spatio-temporal demodulation of $N-$step 2×2 pixelated phase-shifted interferograms ($N = 1, 2, 3, \ldots$), which allows us to reject the same harmonics as a temporal LS-PSA with $4 \times N$ phase-steps.

Chapter 5

Conclusions and future work

In this dissertation work we analyzed several phase-demodulation methods for pixelated phase-shifted (PPS) interferograms. We demonstrated that the synchronous demodulation method is the simplest and yet more convenient phase-demodulation approach for PPS interferograms, we deduced its previously unknown figures of merit and reported several algorithmic approaches to improve its robustness.

In Chapter 1 we highlighted the importance of single-image phase-shifting interferometry. Then in Chapter 2 we demonstrated that the synchronous demodulation method is the simplest and yet more convenient approach to demodulate PPS interferograms. We also introduced a mathematical model for the 2-D pixelated carrier, which is the first novel contribution in this dissertation work and a fundamental piece of information in order to understand the non-linear spectral behavior of this synchronous demodulation method.

In Chapter 3 we analyzed the most commonly observed systematic errors in interferometry (additive noise, detuning error and high-order distorting harmonics) and their consequence for pixelated phase-shifted modulation. To deal with significant amounts of additive noise we proposed a general formula for valid averaging masks to be used in high performance low-pass filtering for 2×2 unit-cell configurations. We also shown that the detuning-error in PPS interferometry results into a spurious, high-frequency additive signal into the estimated phase, and we proposed a straightforward algorithmic approach to cope with this spurious contribution during the calibration process. On the other hand, we shown that the synchronous demodulation of 2×2 unit-cell PPS interferograms has identical harmonics-rejection capabilities as the 4-step LS-PSA, which is the theoretical maximum for the given number of phase-shifted samples.

In Chapter 4, two experimental variants were proposed to enhance the harmonics rejection capability of the pixelated phase-shifted technique: increasing the number of the phase-shifted samples and spatio-temporal phase demodulation. In the first case, we found

that a pixelated phase-mask with a 3×3 unit-cell following a "spiral" configuration allows us to emulate the spectral behavior of the 9-step LS-PSA. However, the main disadvantage of this approach is that requires manufacturing a new (and more complex) type of pixelated phase-masks. As alternative to these complex pixelated phase-mask configurations, we demonstrated that few-steps temporal PSI techniques allow us to reject the distorting harmonics that remain at the base-band after the spatial synchronous demodulation process is applied: the $\{-3^{\text{rd}}, 5^{\text{th}}, -7^{\text{th}}, 9^{\text{th}}, ...\}$ ones. We proposed two custom-made temporal PSAs with 2 and 3 steps designed to remove (at least) the $\{-3^{\text{rd}}, 5^{\text{th}}\}$ and $\{-3^{\text{rd}}, 5^{\text{th}}, -7^{\text{th}}, 9^{\text{th}}\}$ complex harmonics, respectively. As it was demonstrated mathematically and numerically, the spatio-temporal demodulation (that is, the spatial synchronous demodulation of 2×2 unit-cell PPS interferograms together with $N-$step temporal quadrature filtering) is as robust against distorting harmonic as a $4N$-step LS-PSA.

Although our above listed conclusions were confirmed by our numerical simulations, for the moment we have not tested our algorithms in real-world experiments. We believe the next step is, first and foremost, to perform non-simulated physical tests because the experiment could reveal parameters and variables that may not have been considered in our mathematical model. Future perspectives of this research line may include multiple wavelength processing, temporal phase-unwrapping, applications to physical phenomena where the signal of interest is modulated in amplitude, and so on.

Acknowledgments

- To my friends and family.
- To my thesis advisers and fellow students.
- To the hard-working staff of the CIO.
- To my examining committee for your valuable remarks.
- Special thanks to the Mexican National Council of Science and Technology (CONACYT) for the financial support.

Bibliography

[1] Yasuhiro Awatsuji, Atsushi Fujii, Toshihiro Kubota, and Osamu Matoba. Parallel three-step phase-shifting digital holography. *Appl. Opt.*, 45(13):2995–3002, 2006.

[2] N. J. Brock, J. E. Millerd, J. C. Wyant, and J. B. Hayes. Pixelated phase-mask interferometer, 2007. US Patent 7,230,717.

[3] Neal Brock, John Hayes, Brad Kimbrough, James Millerd, Michael North-Morris, Matt Novak, and James C. Wyant. Dynamic interferometry. *Proc. SPIE*, 5875:58750F–58750F–10, 2005.

[4] J. H. Bruning, Donald R. Herriott, J. E. Gallagher, D. P. Rosenfeld, A. D. White, and D. J Brangaccio. Digital wavefront measuring interferometer for testing optical surfaces and lenses. *Appl. Opt.*, 13(11):2693–2703, 1974.

[5] P. Carré. Installation et utilisation du comparateur photoelectrique et interferentiel du bureau international des poids et mesures. *Metrologia*, 2:13–23, 1966.

[6] R. Crane. Interference phase measurement. *Appl. Opt.*, 8:538, 1969.

[7] K. Creath. Phase measuring interferometry: Beware of these errors. *Proc. SPIE*, 1559:313–220, 1991.

[8] K. Freischlad and C. L. Koliopoulos. Fourier description of digital phase-measuring interferometry. *J. Opt. Soc. Am. A*, 7(4):542–551, 1990.

[9] Dennis C. Ghiglia and Mark D. Pritt. *Two-dimensional Phase Unwrapping; Theory, Algoritms, and Software*. Wiley-Interscience, 1998.

[10] Kjell J. Gåsvik. *Optical Metrology*. John Wiley & Sons, 3rd edition, 2002. ISBN: 978-0-470-84670-4.

[11] Y. Ichioka and M. Inuiya. Direct phase detecting system. *Appl. Opt.*, 11:1507–1514, 1972.

[12] B. Kimbrough. Pixelated mask spatial carrier phase shifting interferometry algorithms and associated errors. *Appl. Opt.*, 45(19):4554–4562, 2006.

[13] Brad Kimbrough, Neal Brock, and James Millerd. Dynamic surface roughness profiler. *Proc. SPIE*, 8501:85010D–85010D–12, 2012.

[14] Brad Kimbrough and James Millerd. The spatial frequency response and resolution limitations of pixelated mask spatial carrier based phase shifting interferometry. *Proc. SPIE*, 7790:77900K–77900K–12, 2010.

[15] Malgorzata Kujawinska. New challenges for optical metrology: Evolution or revolution. In Wolfgang Osten, editor, *Fringe 2005*, pages 14–29. Springer Berlin Heidelberg, 2006.

[16] K. G. Larkin and B. F. Oreb. Design and assessment of symmetrical phase-shifting algorithms. *J. Opt. Soc. Am. A*, 9(10):1740–1748, 1992.

[17] Bo Li, Lei Chen, Chen Xu, and Jinpeng Li. The simultaneous suppression of phase shift error and harmonics in the phase shifting interferometry using carrier squeezing interferometry. *Optics Communications*, 296(0):17–24, 2013.

[18] Wu-Sheng Lu and Andreas Antoniou. *Two-Dimensional Digital Filters*. Marcel Dekker Inc., 1992.

[19] James Millerd, Neal Brock, John Hayes, Brad Kimbrough, Matt Novak, Michael North-Morris, and James C. Wyant. Modern approaches in phase measuring metrology (invited paper). *Proc. SPIE*, 5856:14–22, 2005.

[20] James E. Millerd. Linear-carrier phase-mask interferometer, 2013. US Patent 8,351,048.

[21] James E. Millerd, Neal J. Brock, John B. Hayes, Michael B. North-Morris, Matt Novak, and James C. Wyant. Pixelated phase-mask dynamic interferometer. *Proc. SPIE*, 5531:304–314, 2004.

[22] Miguel A. Navarro, Julio C. Estrada, M. Servin, Juan A. Quiroga, and Javier Vargas. Fast two-dimensional simultaneous phase unwrapping and low-pass filtering. *Opt. Express*, 20(3):2556–2561, January 2012.

[23] Matt Novak, James Millerd, Neal Brock, Michael North-Morris, John Hayes, and James Wyant. Analysis of a micropolarizer array-based simultaneous phase-shifting interferometer. *Appl. Opt.*, 44(32):6861–6868, 2005.

[24] J. M. Padilla, M. Servin, and J. C. Estrada. Harmonics rejection in pixelated interferograms using spatio-temporal demodulation. *Opt. Express*, 19(20):19508–19513, 2011.

[25] J. M. Padilla, M. Servin, and J. C. Estrada. Synchronous phase-demodulation and harmonic rejection of 9-step pixelated dynamic interferograms. *Opt. Express*, 20:11734–11739, 2012.

[26] J. M. Padilla, M. Servin, J. C. Estrada, and C. A. Gonzalez. Towards a general theory for MxN pixelated carrier interferometry. *Proc. SPIE*, 8493:849315–849315–9, 2012.

[27] Athanasios Papoulis and S. Unnikrishna Pillai. *Probability, Random Variables and Stochastic Processes*. McGraw-Hill, 4th edition, 2002. ISBN-13: 978-0071199810.

[28] Gustavo Rodriguez-Zurita, Noel-Ivan Toto-Arellano, Cruz Meneses-Fabian, and José F Vázquez-Castillo. One-shot phase-shifting interferometry: five, seven, and nine interferograms. *Opt. Lett.*, 33(23):2788–2790, 2008.

[29] Horst Schreiber and John H. Bruning. *Phase Shifting Interferometry*, chapter 14, pages 547–666. John Wiley & Sons, Inc., 2006.

[30] J. Schwider, R. Burow, K. E. Elssner, J. Grzanna, R. Spolaczyk, and K. Merkel. Digital wave-front measuring interferometry: some systematic error sources. *Appl. Opt.*, 22(21):3421, November 1983.

[31] M. Servin and J. C. Estrada. Error-free demodulation of pixelated carrier frequency interferograms. *Optics Express*, 18(17):18492–18497, August 2010.

[32] M. Servin, J. C. Estrada, and O. Medina. Fourier transform demodulation of pixelated phase-masked interferograms. *Optics Express*, 18(15):16090–16095, July 2010.

[33] M. Servin, J. C. Estrada, and J. A. Quiroga. The general theory of phase shifting algorithms. *Opt. Express*, 17(24):21867–21881, Nov 2009.

[34] M. Servin, J. A. Quiroga, and J. M. Padilla. *Fringe Pattern Analysis for Optical Metrology: theory, algorithms and applications*. Wiley-VCH. Forthcoming 2014.

[35] Manuel Servin and Malgorzata Kujawinska. *Modern Fringe Pattern Analysis in Interferometry*, chapter 12, pages 373–426. Marcel Dekker, Inc., 2001.

[36] Y. Surrel. Design of algorithms for phase measurements by the use of phase stepping. *Appl. Opt.*, 35(1):51–60, 1996.

[37] Mitsuo Takeda, Hideki Ina, and Seiji Kobayashi. Fourier-transform method of fringe-pattern analysis for computer-based topography and interferometry. *J. Opt. Soc. Am.*, 72(1):156–160, Jan 1982.

[38] A. N. Tikhonov and V. Y. Arsenin. *Solutions of ill-posed problems*. Winston, 1977.

[39] J. C. Wyant. Use of an ac heterodyne lateral shear interferometer with real-time wavefront correction systems. *Appl. Opt.*, 14(11):2622–2628, 1975.

[40] James C. Wyant. Dynamic interferometry. *Optics and photonics news*, 14(4):36–41, 2003.

Appendix A

Related publications

For the reader's convenience and for ease of reference, the physical version of this document ends with a printed version of Padilla et al. [24, 25, 26].